
**FEDERAL UNIVERSITY OF CEARÁ**

**CENTER OF SCIENCE**

**DEPARTMENT OF PHYSICS**

**POST-GRADUATION PROGRAM IN PHYSICS**

**MASTER DEGREE IN PHYSICS**

**OTÁVIO PEIXOTO FURTADO**

# LOW-TEMPERATURE STRUCTURAL PHASE TRANSITIONS OF THE LEAD-FREE HYBRID VACANCY-ORDERED PEROVSKITE $(DMA)_2SnBr_6$

**FORTALEZA**

**2023**

OTÁVIO PEIXOTO FURTADO

# LOW-TEMPERATURE STRUCTURAL PHASE TRANSITIONS OF THE LEAD-FREE HYBRID VACANCY-ORDERED PEROVSKITE $(DMA)_2SnBr_6$

Dissertation submitted to the Post-Graduation Program in Physics of the Center of Science of the Federal University of Ceará, as a partial requirement for obtaining the title of Master in Physics. Concentration Area: Condensed Matter Physics.

Advisor: Prof. Dr. Alejandro Pedro Ayala

FORTALEZA

2023

Dados Internacionais de Catalogação na Publicação
Universidade Federal do Ceará
Sistema de Bibliotecas
Gerada automaticamente pelo módulo Catalog, mediante os dados fornecidos pelo(a) autor(a)

---

F988l Furtado, Otávio Peixoto.
Low-temperature structural phase transitions of the lead-free hybrid vacancy-ordered perovskite (DMA)2SnBr6 / Otávio Peixoto Furtado. – 2023.
59 f. : il. color.

Dissertação (mestrado) – Universidade Federal do Ceará, Centro de Ciências, Programa de Pós-Graduação em Física, Fortaleza, 2023.
Orientação: Prof. Dr. Alejandro Pedro Ayala.

1. Hybrid Perovskite. 2. Phase Transition. 3. Single Crystal X-Ray Diffraction. 4. Raman Spectroscopy. I. Título.

CDD 530

---

OTÁVIO PEIXOTO FURTADO

# LOW-TEMPERATURE STRUCTURAL PHASE TRANSITIONS OF THE LEAD-FREE HYBRID VACANCY-ORDERED PEROVSKITE $(DMA)_2SnBr_6$

Dissertation submitted to the Post-Graduation Program in Physics of the Center of Science of the Federal University of Ceará, as a partial requirement for obtaining the title of Master in Physics. Concentration Area: Condensed Matter Physics.

Approved on: 25th September 2023

EXAMINATION BOARD

---

Prof. Dr. Alejandro Pedro Ayala (Advisor)
Federal University of Ceará (UFC)

---

Prof. Dr. Dieric dos Santos de Abreu
Federal University of Ceará (UFC)

---

Dr. Bruno Sousa Araújo
Federal University of Ceará (UFC)

I dedicate this work to my family and all of those who supported through this scientific journey.

## ACKNOWLEDGEMENTS

Firstly, I would like to thank my parents Jocyrregia Maria and Gerardo Fabiano as well as my wife Isis do Vale Meira Lima and my entire family for their great support throughout the develoment of this work.

I also thank the Federal University of Ceará (UFC) for providing me with a productive environment, high—quality education and excellent infrastructure, whether in the classrooms or in the research laboratories. Secondly, I am grateful to the Postgraduate Program in Physics, the professors, secretaries, and the coordinators who provided support and instructed me during this important stage of the Academic Master's degree. This study was financed by the Conselho Nacional de Desenvolvimento Científico e Tecnológico — Brasil (CNPq).

In particular, I would also like to deeply thank Prof. Dr. Alejandro Pedro Ayala for his excellent mentoring, respect, professionalism, and for all the support he has given to me, as well as Dr. Mayra Alexandra Padrón Gómez for her great contribution with the experimental results of this work and Dr. Juan Simón Rodríguez Hernández, both also hold a great part in the development of this work and in my formation as a physicist since my undergraduate studies.

Finally I would like to express my sincere appreciation to the members of the Structural Crystalography Laboratory (LabCrEs) at UFC for their support. All of you possess remarkable talent and wherever I go, I will hope for your success. Lastly, I am very grateful to the invited professors who agreed to participate in the examining board, Prof. Dr. Dieric dos Santos de Abreu and Dr. Bruno Sousa Araújo, for their availability, valuable contributions and suggestions to this work.

The study of physics is also an adventure. You will find it challenging, sometimes frustrating, occasionally painful, and often richly rewarding.

(YOUNG, 1999)

## ABSTRACT

In this master's thesis, a combination of experimental and theoretical techniques are employed to investigate the hybrid lead-free vacancy-ordered perovskite material $[(CH_3)_2NH_2]_2SnBr_6$ (or in its abbreviated form: $(DMA)_2SnBr_6$) and its structural changes that happen at low temperatures. Through the use of experimental techniques such as Single Crystal X-Ray Diffraction (SCXRD), Differential Scanning Calorimetry (DSC) and Raman spectroscopy, it was possible to identify that this compound undergoes three structural phase transitions near the temperatures of 200 K, 100 K and 50 K. The first two transitions were found in our SCXRD measurements, with the first one being a displacive orthorhombic-monoclinic phase transition, while the second one was found to be an order-disorder monoclinic-triclinic phase transition. The last transition was only observed experimentaly through our Raman spectroscopy measurements and was confirmed as a triclinic-triclinic phase transition based on our theoretical Γ-point phonon calculation.



**Keywords:** lead-free perovskite; phase transition;single crystal x-ray diffraction; Raman spectroscopy

## RESUMO

Nesta dissertação de mestrado, uma combinação de técnicas experimentais e teóricas são utilizadas para investigar as propriedades da perovskita híbrida, livre de chumbo e ordenada por vacância $[(CH_3)_2NH_2]_2\ SnBr_6$ (ou na forma abreviada: $(DMA)_2SnBr_6$) e suas mudanças estruturais que ocorrem em baixas temperaturas. A partir do uso de técnicas experimentais como Difração de Raios-x de Monocristal (SCXRD), Calorimetria de Varredura Diferencial (DSC) e espectroscopia Raman, foi possivel identificar as transições de fase proximas às temperaturas de 200 K, 100 K e 50 K. As duas primeiras transições foram identificadas em nossas medidas de SCXRD, onde a primeira foi identificada como uma transição do tipo displaciva ortorrômbico-monoclínico, enquanto a segunda foi descoberta como uma transição ordem-desordem monoclínico-triclínico. A última transição foi observada experimentalmente apenas através das nossas medidas de espectroscopia Raman e foi confimada como uma transição triclínica-triclínica a partir dos nossos cálculos teóricos de fônons no ponto $\Gamma$.



**Palavras-chave:** perovskita livre de chumbo; transição de fase; difração de raios-x de monocristal; espectroscopia Raman

## LIST OF FIGURES

## LIST OF TABLES

## LIST OF SYMBOLS

| | |
|---|---|
| $\boldsymbol{E}$ | electric field vector |
| $\nu_0$ | Frequency of incident radiation |
| $\boldsymbol{M}$ | electric dipole moment |
| $H$ | Hamiltonian operator |
| $\Psi$ | time-dependent solution of the Schrödinger equation |
| $\boldsymbol{Q_m}$ | normal coordinate of the m-th vibrational mode |
| $\sigma$ | octahedron Angular deformation |
| $\Delta d$ | octahedron bond-length deformation |

**CONTENTS**

# 1 INTRODUCTION

Halide perovskite semiconductors have marked the last years with their promising properties that emerge in both their hybrid and inorganic variants, with Lead Halide Perovskites (LHPs) getting the spotlight for the prospects of their application in optoelectronic devices, most prominently as active layers of solar cells. However, recently many advances have been made in attempts to replace the lead (Pb) in order to reduce the health risks caused by its toxicity. Among the alternatives, the tin (Sn) based halide perovskites (THPs) present themselves as very favorable candidates due to having similar ionic radius and similar electronic structure to that of lead (CHOWDHURY *et al.*, 2022), with recent studies already surpassing a power conversion efficiency (PCE) of 13% on a Sn-based perovskite solar cell (NISHIMURA *et al.*, 2020).

Nevertheless, the THPs still face strong drawbacks that stop its widespread application in solar harvesting devices, with one of the main ones being the chemical instability the of tin arising from the oxidation of the $Sn^{2+}$, usually present in the B cation site on the classical perovskite structures ($ABX_3$), to its $Sn^{4+}$ state, leading to an unwanted p-type self-doping that increases charge carrier recombination and furthermore reduces carrier diffusion lengths (NOEL *et al.*, 2014; RICCIARELLI *et al.*, 2020). In order to deal with the instability of the THPs, methods such as the dimensionality reduction through the replacement of the A-site cation by large organic cations like butylammonium ($[C_4H_9NH_3]^+$, or BA) and phenylethylammonium ($[C_6H_5(CH_2)_2NH_3]^+$, or PEA) (LIAO *et al.*, 2017; ZHU *et al.*, 2022) or the incorporation of reducing agents such as $SnX_2$ (X = F, Cl, Br, I) (WANG; YAN, 2020; SONG *et al.*, 2017) or hydrazine ($N_2H_4$) (SONG *et al.*, 2017) have been moderately successfull, however a different variety of the perovskite structure known as vacancy-ordered double perovskites ($A_2BX_6$) have emerged as potential solution since tin can be incorporated in its more stable $Sn^{4+}$ oxidation state (GLOCKZIN *et al.*, 2023; BHUMLA *et al.*, 2022) and studies already show the potential optoelectronic applications of the all inorganic $Cs_2SnX_6$ (X = I,Cs) (LEE *et al.*, 2014; FAIZAN *et al.*, 2021a; TAN *et al.*, 2018).

In this work, the hybrid vacancy-ordered tin-based perovskite material named bis (Dimethylammonium) hexabromo-stannate(iv): $[(CH_3)_2NH_2]_2SnBr_6$ or in its abbreviated form: $(DMA)_2SnBr_6$ (DMA = $[(CH_3)_2NH_2]^+$), was comprehensively analyzed through its structural-property changes under low-temperature conditions. Several experimental characterization techniques, including Single Crystal X-Ray Diffraction (SCXRD), Differential Scanning Calorimetry (DSC) and Raman spectroscopy were all employed to understand and characterize its properties.

# 2 THEORETICAL FRAMEWORK

## 2.1 The perovskite structure

The term "perovskite" was originally attributed to the calcium titanite ($CaTiO_3$) mineral, initially discovered on the Ural Mountains of Russia. This mineral‘s name was coined by the German mineralogist and crystallographer Gustav Rose, who named it after the Russian politician and mineralogist Lev Perovski (KATZ, 2020). At ambient temperature, the crystal structure of $CaTiO_3$ can be described as the periodic repetition of the corner-sharing $[TiO6]^{2-}$ octahedrons formed by the $Ti^{4+}$ cations surrounded by six $O^{2-}$ anions. Meanwhile, the $Ca^{2+}$ cations are found in the vacant spaces left by the octahedra (see Figure 1). Recently, many coordination polymers have been classified as perovskites due to structural similarities with this mineral. Many of these compounds are generally described the same general chemical formula $ABX_3$, where typically, A is a cation with an ionic radius larger that B and X is an anion, usually a halide or the oxygen anion $O^{2-}$. The ideal structure of a simple perovskite has a cubic symmetry and is shown on Figure 1.

Figure 1 – The representation of the simple perovskite structure

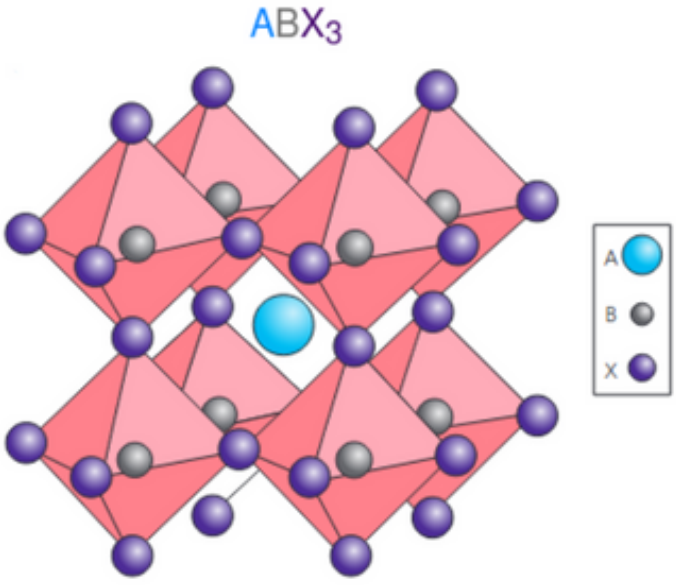


Source: Adapted from Green et al. (GREEN *et al.*, 2014)

Recently, perovskites have been attracting a lot of attention, due to properties such as: high absorption coefficient, adjustable optical band gap, low exciton binding energies and long charge carrier diffusion lengths (ALTINKAYA *et al.*, 2021; NOH *et al.*, 2013; DONG *et al.*,

2015; SNAITH, 2013), which makes these materials ideal candidates for optoelectronic devices, such as light emitting diodes (LEDs), photodetectors, lasers and especially the perovskite solar cells (PSCs).

However, even though there is a large set of materials that can be classified as the simple $ABX_3$ perovskites, the geometrical restrictions of this structure impose certain limitations over the possible choices of elements that can be incorporated. One of the most important quantities related to these limitations is the Goldschmidt tolerance factor, given by (GOLDSCHMIDT, 1926):

$$t = \frac{R_A + R_X}{\sqrt{2}(R_B + R_X)}$$

where $R_A$, $R_B$ e $R_X$ are the ionic radii of the A, B e X ions, respectively. In this way, the stability of a potential simple perovskite, formed by the given A, B and X elements, can be predicted by using the fact that, generally, a stable perovskite structure lies in the range $0.8 \leq t \leq 1$, with $t = 1$ being the ideal cubic structure. This condition has a simple interpretation: in cases where $t > 1$, the A-site cation is too large when compared to the B-site cation and, in this case, usually the final structure is formed by layers of octahedrons separated by the (usually organic) A-site cation (KIESLICH *et al.*, 2014; BURGER *et al.*, 2018) or, in some cases, different non-perovskite structures become more energetically favorable, as is the case of $FAPbI_3$, which is a compound that has a photoactive $\alpha-FAPbI_3$ perovskite phase, however it is less stable than its $\delta-FAPbI_3$ non-perovskite phase (LIU *et al.*, 2017). In cases where $t < 0.8$, the A-site cation is too small and its size becomes more similar to the B-site cation, leading to the formation of the ilmenite-type (FeTiO3) structures (KIESLICH *et al.*, 2014).

Because of these geometric limitations, in order to explore new routes for materials with similarly desirable properties, it becomes necessary to divert from the simple $ABX_3$ perovskite formula. In this perspective, an interesting route that has been explored is the one of the double perovskites (KHALFIN; BEKENSTEIN, 2019), with the general chemical formula $A_2BB'X_6$, where the B-site cation has been replaced by the two different cations with different oxidation states in order to maintain the charge balance. The double perovskite structure is shown in Figure 2.

Figure 2 – The representation of the double perovskite structure

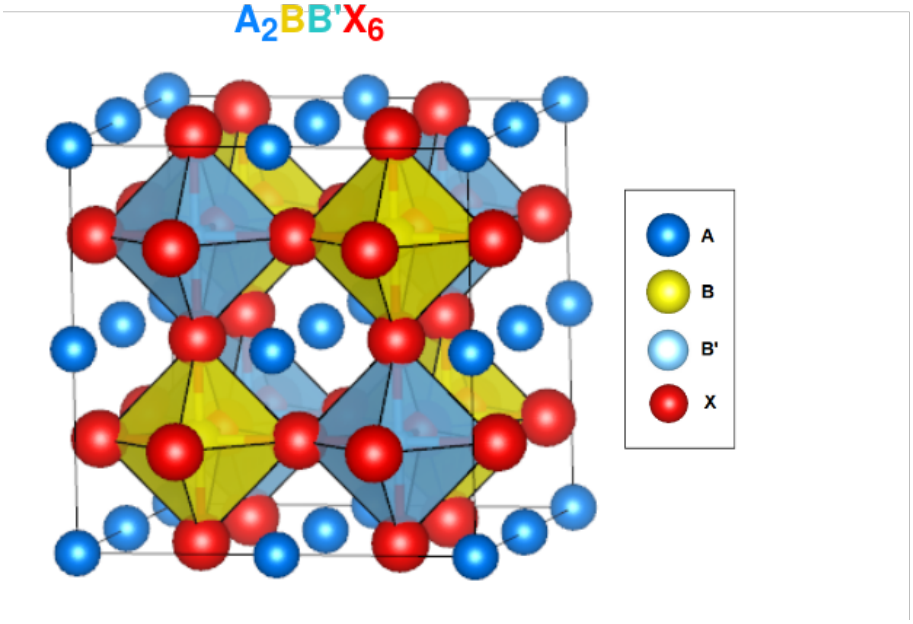


Source: Created by the author

The double perovskite structure will still face similar geometric limitations, however, their composition is much more tunable due to the possibility of choosing two different cations for the B-site, which results in a large amount of new potential candidates for optoelectronic applications. Among them, $Cs_2InSbCl_6$, $Cs_2AgInBr_6$, $Rb_2AgInBr_6$, and $Rb_2CuInCl_6$ have shown great potential for their high theoretical efficiencies as perovskite solar cell active layers (ZHAO *et al.*, 2017).

On a similar note, the perovskite structures known as vacancy-ordered double perovskite has been considered as an interesting alternative. Their structure is very similar to the one of a double perovskite, however, instead of using two different cations for the B-site, a single cation with higher oxidation state (usually a +4 state) is used, which causes half of the B-sites to be occupied and the other half to be vacant (see Figure 3a)) (MAUGHAN *et al.*, 2019a; FAIZAN *et al.*, 2022). This family of perovskite structures has been offering new opportunities for environmentally friendly solar cell materials with interesting properties and diverse compositions, such as: $Rb_2PdI_6$, $Rb_2PdBr_6$, $Cs_2PtI_6$ and $Cs_2SnX_6$ (X = Cl, Br, I), which show high carrier mobility and adjustable bandgaps in the visible range, while being lead-free (FAIZAN *et al.*, 2021b; KALTZOGLOU *et al.*, 2016).

Figure 3 – Comparison between simple, double and vacancy-ordered perovskite structures

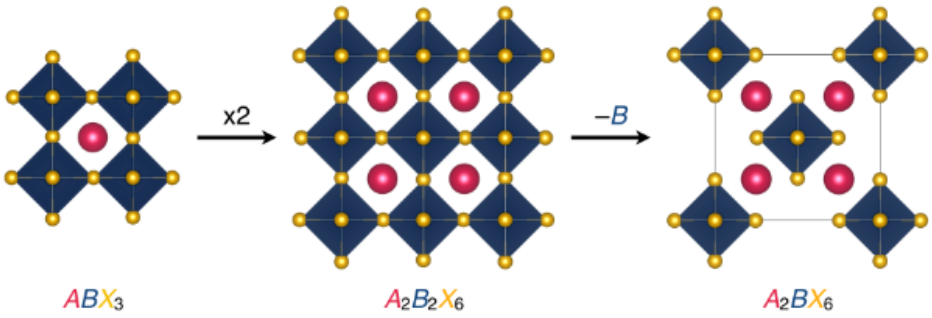


Source: Adapted from Maughan et al. (MAUGHAN *et al.*, 2019b)

## 2.2 Raman Scattering Theory

We will consider the case where a system of atoms interacts with an unpolarized incident radiation with an electric field $\boldsymbol{E}$ expressed as:

$$\boldsymbol{E} = \boldsymbol{A}e^{-2\pi i\nu_0 t} + \boldsymbol{A}^* e^{2\pi i\nu_0 t} \tag{2.1}$$

The $\boldsymbol{A}$ and $\boldsymbol{A}^*$ represent a complex vector and its conjugate, this way we guarantee that expression 2.1 is real, since if $\boldsymbol{A} = \boldsymbol{a} + i\boldsymbol{b}$ ($\boldsymbol{a}$ and $\boldsymbol{b}$ being real vectors), then we get:

$$\boldsymbol{E} = 2(\boldsymbol{a}\cos(2\pi\nu_0 t) + \boldsymbol{b}\sin(2\pi\nu_0 t))$$

### *2.2.1 First-order perturbation theory*

When interacting with the system, this electric field produces an induced dipole moment $\mathbf{M}$ which in turn creates a perturbing potential $H^1 = -\boldsymbol{M}\cdot\boldsymbol{E}$ and the time-dependent Schrödinger equation of the perturbed system can be written as:

$$(H^0 - \boldsymbol{M}\cdot\boldsymbol{E})\Psi(q,t) = -\frac{\hbar}{i}\frac{\partial\Psi}{\partial t}(q,t) \tag{2.2}$$

where $H^0$ is the Hamiltonian of the unperturbed system. Using the first-order perturbation theory (COHEN-TANNOUDJI *et al.*, 2019), we can express the perturbed wave function of the kth state as :

$$\Psi_k(q,t) = \Psi_k^0(q,t) + \Psi_k^1(q,t) \tag{2.3}$$

where $\Psi_k^0(q,t)$ represents the solution to the unperturbed Schrödinger equation:

$$H^0\Psi_k^0(q,t) = -\frac{\hbar}{i}\frac{\partial\Psi_k^0}{\partial t}(q,t) \tag{2.4}$$

Therefore we can write that $\Psi_k^0(q,t) = \psi_k(q)e^{-\frac{i}{\hbar}E_k^0 t}$, with $\psi_k(q)$ being the solution of the unperturbed time-independent Schrödinger equation:

$$H^0\psi_k(q) = E_k^0\psi_k(q)$$

Using equations 2.3 and 2.4, equation 2.2 can be rewritten as:

$$\left(H^0 - \frac{\hbar}{i}\frac{\partial}{\partial t}\right)\Psi_k^1(q,t) = (\boldsymbol{E}\cdot\boldsymbol{M})\Psi_k^0(q,t) = (\boldsymbol{E}\cdot\boldsymbol{M})\psi_k(q)e^{-\frac{i}{\hbar}E_k^0 t} \tag{2.5}$$

and by replacing equation 2.1 in 2.5 we get:

$$\left(H^0 - \frac{\hbar}{i}\frac{\partial}{\partial t}\right)\Psi_k^1(q,t) = (\boldsymbol{A}\cdot\boldsymbol{M})\psi_k(q)e^{-\frac{i}{\hbar}(E_k^0+h\nu_0)t} + (\boldsymbol{A}^*\cdot\boldsymbol{M})\psi_k(q)e^{-\frac{i}{\hbar}(E_k^0-h\nu_0)t} \tag{2.6}$$

which has a solution of the form:

$$\Psi_k^1(q,t) = \psi_k^+(q)e^{-\frac{i}{\hbar}(E_k^0+h\nu_0)t} + \psi_k^-(q)e^{-\frac{i}{\hbar}(E_k^0-h\nu_0)t} \tag{2.7}$$

where $\psi_k^+(q)$ and $\psi_k^-(q)$ can be obtained from:

$$H^0\psi_k^+(q) - (E_k^0 + h\nu_0)\psi_k^+(q) = (\boldsymbol{A}\cdot\boldsymbol{M})\psi_k(q) \tag{2.8}$$

$$H^0\psi_k^-(q) - (E_k^0 - h\nu_0)\psi_k^-(q) = (\boldsymbol{A}^*\cdot\boldsymbol{M})\psi_k(q) \tag{2.9}$$

Considering that, in the unperturbed state, the dipole moment operator has matrix elements of the form $\overline{M}_{kr} = \int \psi_r^* \boldsymbol{M}\psi_k dq$, the right side of equations 2.8 and 2.9 can be written in the form:

$$(\boldsymbol{A}\cdot\boldsymbol{M})\psi_k(q) = \sum_r (\boldsymbol{A}\cdot\overline{M}_{kr})\psi_r(q)$$

By writing the time-independent perturbed functions ($\psi_k^+(q)$ and $\psi_k^-(q)$) as linear combinations of the unperturbed wave functions ($\psi_r(q)$):

$$\psi_k^{\pm} = \sum_r a_{kr}^{\pm} \psi_r(q) \tag{2.10}$$

and then replacing 2.10 in 2.8 and 2.9 we can obtain:

$$\psi_k^{+} = \sum_r \frac{\boldsymbol{A} \cdot \overline{M}_{kr}}{E_r^0 - E_k^0 - h\nu_0} \psi_r(q) \tag{2.11}$$

$$\psi_k^{-} = \sum_r \frac{\boldsymbol{A}^* \cdot \overline{M}_{kr}}{E_r^0 - E_k^0 + h\nu_0} \psi_r(q) \tag{2.12}$$

Hence, when using that: $E_r^0 - E_k^0 = h\nu_{rk}$ the expression for the perturbation term in the wave function can be written as:

$$\Psi_k^1(q,t) = \frac{1}{h} \sum_r \psi_r(q) \left[ \frac{\boldsymbol{A} \cdot \overline{M}_{kr}}{\nu_{rk} - \nu_0} e^{-\frac{i}{\hbar}(E_k^0 + h\nu_0)t} + \frac{\boldsymbol{A}^* \cdot \overline{M}_{kr}}{\nu_{rk} + \nu_0} e^{-\frac{i}{\hbar}(E_k^0 - h\nu_0)t} \right] \tag{2.13}$$

and now, the time-dependent dipole moments associated with the transition k -> n can be calculated following that:

$$\boldsymbol{M}_{kn} = \int \Psi_n^* \boldsymbol{M} \Psi_k dq = \int (\Psi_n^0 + \Psi_n^1)^* \boldsymbol{M} (\Psi_k^0 + \Psi_k^1) dq \tag{2.14}$$

### *2.2.2 Rayleight scattering*

For the simplest case, when the final state is equal to the initial state ($n = k$), we have:

$$\boldsymbol{M}_{kk} = \overline{M}_{kk} + (\boldsymbol{C}_{kk} e^{-2\pi i \nu_0 t} + \boldsymbol{C}_{kk}^* e^{2\pi i \nu_0 t}) \tag{2.15}$$

Where the first term ($\overline{M}_{kk}$) was previously mentioned and is a time-independent unperturbed permanent dipole moment present in the system, while $\boldsymbol{C}_{kk}$ is given by:

$$\boldsymbol{C}_{kk} = \frac{1}{h} \sum_r \left[ \frac{(\boldsymbol{A} \cdot \overline{M}_{kr}) \overline{M}_{rk}}{\nu_{rk} - \nu_0} + \frac{\overline{M}_{kr} (\boldsymbol{A} \cdot \overline{M}_{rk})}{\nu_{rk} + \nu_0} \right]$$

Upon inspecting the second term (in parenthesis) in equation 2.15, it is easily seen that it shares a similar form to the incident incoming light (equation 2.1) and its the term that represents the coherent Rayleigh scattering.

### *2.2.3 Raman scattering*

Now considering two different states ($n \neq k$), in this case the transition dipole moment can be divided in three terms:

$$\boldsymbol{M}_{kn} = \boldsymbol{M}^{\mathbf{0}}_{kn} + \boldsymbol{M}^{\mathbf{1}}_{kn} + \boldsymbol{M}^{\mathbf{2}}_{kn} \tag{2.16}$$

where:

$$\boldsymbol{M}^{\mathbf{0}}_{kn} = \overline{M}_{kn} e^{-2\pi i \nu_{kn} t} \tag{2.17}$$

$$\begin{aligned} \boldsymbol{M}^{\mathbf{1}}_{kn} = & \frac{1}{h} \sum_r \left[ \frac{(\boldsymbol{A} \cdot \overline{M}_{kr}) \overline{M}_{rn}}{\nu_{rk} - \nu_0} + \frac{\overline{M}_{kr} (\boldsymbol{A} \cdot \overline{M}_{rn})}{\nu_{rn} + \nu_0} \right] e^{-2\pi i (\nu_{kn} + \nu_0) t} + \\ & + \frac{1}{h} \sum_r \left[ \frac{(\boldsymbol{A}^* \cdot \overline{M}_{kr}) \overline{M}_{rn}}{\nu_{rk} + \nu_0} + \frac{\overline{M}_{kr} (\boldsymbol{A}^* \cdot \overline{M}_{rn})}{\nu_{rn} - \nu_0} \right] e^{-2\pi i (\nu_{kn} - \nu_0) t} \end{aligned} \tag{2.18}$$

$$\begin{aligned} \boldsymbol{M}^{\mathbf{2}}_{kn} = & \frac{1}{h^2} \sum_{r,p} \left[ \frac{(\boldsymbol{A}^* \cdot \overline{M}_{kp}) \overline{M}_{pr} (\boldsymbol{A}^* \cdot \overline{M}_{rn})}{(\nu_{pk} - \nu_0)(\nu_{rn} - \nu_0)} + \frac{(\boldsymbol{A}^* \cdot \overline{M}_{kp}) \overline{M}_{pr} (\boldsymbol{A}^* \cdot \overline{M}_{rn})}{(\nu_{pk} - \nu_0)(\nu_{rn} + \nu_0)} \right] e^{-2\pi i \nu_{kn} t} + \\ & + \frac{1}{h^2} \sum_{r,p} \left[ \frac{(\boldsymbol{A}^* \cdot \overline{M}_{kp}) \overline{M}_{pr} (\boldsymbol{A}^* \cdot \overline{M}_{rn})}{(\nu_{rn} + \nu_0)(\nu_{kp} - \nu_0)} \right] e^{-2\pi i (\nu_{kn} - 2\nu_0) t} \\ & + \frac{1}{h^2} \sum_{r,p} \left[ \frac{(\boldsymbol{A} \cdot \overline{M}_{kp}) \overline{M}_{pr} (\boldsymbol{A} \cdot \overline{M}_{rn})}{(\nu_{rn} - \nu_0)(\nu_{kp} + \nu_0)} \right] e^{-2\pi i (\nu_{kn} + 2\nu_0) t} \end{aligned} \tag{2.19}$$

Each of these components can be written as:

$$\boldsymbol{M}^{\boldsymbol{i}}_{kn} = \left( \overline{M}^{\,i}_{kn} \right) e^{-2\pi i \nu t}$$

which, according to Klein's principle (KLEIN, 1927; PLACZEK, 1959), will correspond to a classical radiating time-dependent dipole moment only if $\nu > 0$. For the first term ($\boldsymbol{M}^{\mathbf{0}}_{kn}$) seen in equation 2.17, this requires that $\nu_{kn} = \nu_k - \nu_n > 0$ and therefore $E_k > E_n$ which represents an induced transition between a higher energy initial state to a lower energy one (see Figure 4 a)).

The second term ($M_{kn}^{1}$) of the transition dipole moment can be seen in equation 2.18 and consists of two parts, the first one corresponds to a classical radiating dipole moment if $\nu_{kn} + \nu_0 > 0$ and in this case the frequency difference $\nu_{kn} = \nu_k - \nu_n$ can assume both positive and negative values which will correspond to the anti-stokes and stokes Raman scattering respectively, while the second part corresponds radiating dipole if $\nu_{kn} - \nu_0 > 0$, which is only accomplished when the system is in excited states of high enough energy such that $h\nu_k - h\nu_n > h\nu_0$.

Its important to note that, in contrast to 2.17 the terms in 2.18 and 2.19 contain sums over all stationary states, which can be interpreted as the system passing through a non-stationary intermediary state, hence it cannot be associated to one single stationary state with defined energy value, but to combination of them. This intermediary state is called a virtual state and would be transient, with the system quickly transitioning into the final state and emitting radiation which, in the case of Raman stokes and anti-stokes scattering will have an energy equal to $E = h(\nu_0 \pm |\nu_{kn}|)$ (see Figure 4 b) and c)).

The third term ($M_{kn}^{2}$) wont be discussed in full detail here, however its third part represents the interaction of the system taking place with two photons of energy $h\nu_0$ with the emission of radiation of frequency $\nu_{kn} + 2\nu_0$ (assuming that $h\nu_n - h\nu_k < 2h\nu_0$ ) and again, the frequency difference $\nu_{kn}$ can be either positive or negative, with this type of scattering being known as the hyper Raman effect (KONINGSTEIN, 2012).

Figure 4 – The depiction of some processes arising from the terms on equation 2.16: a) the induced transition from a higher to a lower energy state arising from 2.17, b) stokes and c) anti-stokes Raman scattering processes.

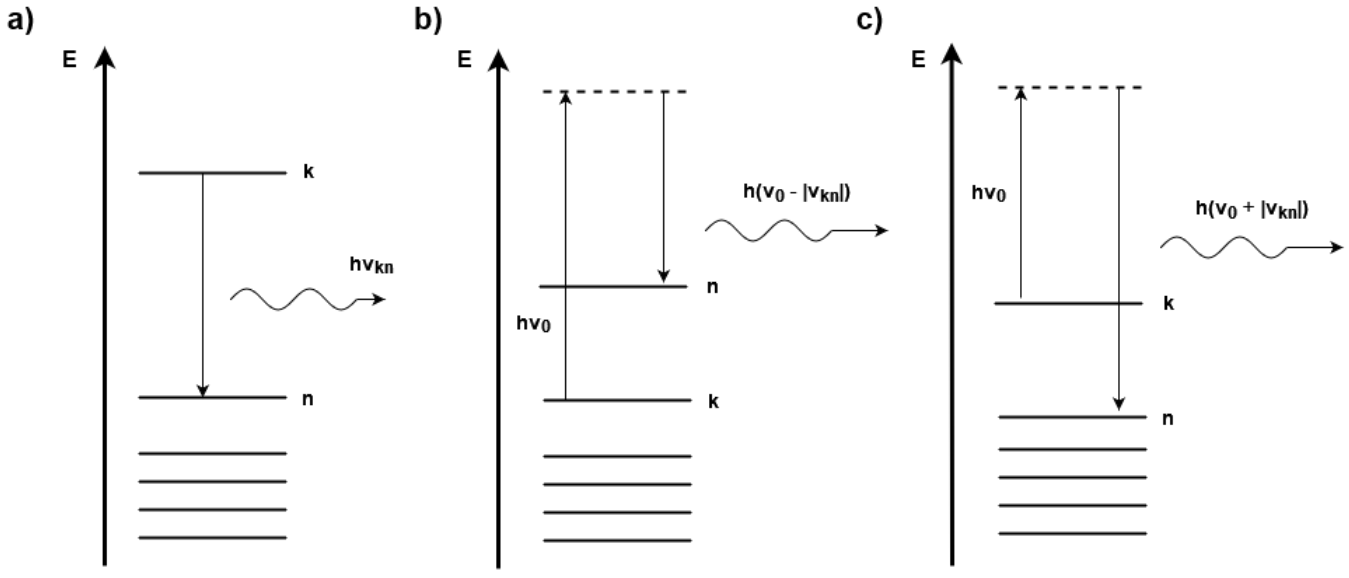


Source: Elaborated by the author

The classical radiating dipole moment associated with the Raman scattering ($\boldsymbol{M}^{\mathbf{1}}_{kn}$) can then be written as a real quantity:

$$\boldsymbol{M}^{\mathbf{1}}_{kn} = \boldsymbol{C}_{kn} e^{-2\pi i(\nu_{kn}+\nu_0)t} + \boldsymbol{C}^{*}_{kn} e^{2\pi i(\nu_{kn}+\nu_0)t} \tag{2.20}$$

where $\boldsymbol{C}_{kn}$ is the complex vector:

$$\boldsymbol{C}_{kn} = \frac{1}{h}\sum_r \left[ \frac{(\boldsymbol{A}\cdot\overline{M}_{kr})\overline{M}_{rn}}{\nu_{rk}-\nu_0} + \frac{\overline{M}_{kr}(\boldsymbol{A}\cdot\overline{M}_{rn})}{\nu_{rn}+\nu_0} \right] \tag{2.21}$$

Each component of $\boldsymbol{C}_{kn}$ can be written as:

$$(\boldsymbol{C}_i)_{kn} = \sum_j (\alpha_{ij})_{kn} A_j \tag{2.22}$$

where $i$ and $j$ stand for the Cartesian components: x,y and z and $(\alpha_{ij})_{kn}$ is the transition polarizability tensor:

$$(\alpha_{ij})_{kn} = \frac{1}{h}\sum_r \left[ \frac{(\overline{M}_j)_{kr}(\overline{M}_i)_{rn}}{\nu_{rk}-\nu_0} + \frac{(\overline{M}_i)_{kr}(\overline{M}_j)_{rn}}{\nu_{rn}+\nu_0} \right] \tag{2.23}$$

In order that a Rayleigh or Raman transition becomes a physically observable quantity, it is a prerequisite that $(\alpha_{ij})_{kn} \neq 0$. The conditions for a non-vanishing polarizability component, also called selection rules, can be derived directly from the symmetry properties of the polarizability operator, which, from the definition of the dipole moment operator as $M_i = \sum_l e_l i$, can be written as:

$$\alpha_{ij} = \frac{1}{h}\sum_r \left[ \frac{\sum_l e_l i\,|\psi_r\rangle\,\langle\psi_r|\sum_l e_l j}{\nu_{rk}-\nu_0} + \frac{\sum_l e_l j\,|\psi_r\rangle\,\langle\psi_r|\sum_l e_l i}{\nu_{rn}+\nu_0} \right] \tag{2.24}$$

This expression shows that $\alpha_{ij}$ will transform under symmetry operations in the same way as the product of coordinates: $i \times j$. By using that $(\alpha_{ij})_{kn} = \langle\psi_n|\,\alpha_{ij}\,|\psi_k\rangle$, we readily see that the transition polarizability is an integral that becomes zero in the case where the product of $\psi_k$, $\psi_n$ and $\alpha_{ij}$ becomes antisymmetric with respect to any of the system's symmetry operations. In other words, the only way to guarantee that $(\alpha_{ij})_{kn} \neq 0$ is if the product of the irreducible representations: $\Gamma_{\psi_n} \times \Gamma_{ij} \times \Gamma_{\psi_k}$ contains a totally symmetric irreducible representation.

### *2.2.4 Vibrational Raman scattering*

Up until this point, the discussion was based on generic quantum states, however in the present work we are interested in the vibrational Raman effect, which arises when the incident radiation interacts with the system and causes a change between vibrational energy levels. In order to treat this specific case we first separate the degrees of freedom of the system into the electron coordinates $\boldsymbol{r}$ and the nuclear vibrational normal coordinates $\boldsymbol{Q_m}$ and then we use the Born-Oppenheimer approximation in order to decouple the electronic wave functions ($\chi(\boldsymbol{r},\boldsymbol{Q_m})$) from the vibrational wave functions ($\phi(\boldsymbol{Q_m})$):

$$\psi(\boldsymbol{r},\boldsymbol{Q_m}) = \chi_k(\boldsymbol{r},\boldsymbol{Q_m})\phi_{v_m}(\boldsymbol{Q_m}) \tag{2.25}$$

The Hamiltonian of the electrons and consequently the electronic wave functions $\chi_k$ cannot be completely decoupled from the nuclei vibrations and therefore will also depend on the vibrational coordinates $\boldsymbol{Q_m}$, however when considering the harmonic approximation of small displacements the electronic Hamiltonian can be expanded around the point $\boldsymbol{Q_m} = 0$ such that:

$$H(\boldsymbol{r},\boldsymbol{Q_m}) \approx H(\boldsymbol{r},\boldsymbol{Q_m}=0) + \left(\frac{\partial H}{\partial \boldsymbol{Q_m}}\right)_{\boldsymbol{Q_m}=0} \boldsymbol{Q_m} \tag{2.26}$$

Since the second term in 2.25 is very small, the same procedure of first-order perturbation theory can be applied if we consider it as the perturbing potential, which results in the perturbed electronic wave functions:

$$\chi_k(\boldsymbol{r},\boldsymbol{Q_m}) = \chi_k^0 + \sum_t h_{tk}^{\boldsymbol{Q_m}} \boldsymbol{Q_m} \chi_t^0 \tag{2.27}$$

where $\chi_k^0 = \chi_k(\boldsymbol{r},\boldsymbol{Q_m}=0)$ and

$$h_{tk}^{\boldsymbol{Q_m}} = \frac{\left\langle \psi_t^0 \right| \frac{\partial H}{\partial \boldsymbol{Q_m}} \left| \psi_k^0 \right\rangle}{E_k^0 - E_t^0}$$

The vibrational wave functions ($\phi_{v_m}(\boldsymbol{Q_m})$) in the harmonic approximations assume the form of the harmonic oscilator solutions:

$$\phi_{v_m}(\boldsymbol{Q_m}) = N_{v_m} e^{-\frac{Q_m^2}{2\alpha}} H_{v_m}(\sqrt{\alpha}\boldsymbol{Q_m}) \tag{2.28}$$

where $N_{v_m}$ is the normalization constant, $\alpha = 4\pi^2 v_m/h$ and $H_{v_m}$ are Hermite polynomials. With the knowledge of the wave functions, the polarizability tensor can be calculated by considering that:

$$(\overline{M}_i)_{kr} = (\overline{M}_i)_{k,v_m;r,v''_m} = \left\langle \chi_r \phi_{v''_m} \middle| M_i \middle| \chi_k \phi_{v_m} \right\rangle = \left\langle \chi_r \phi_{v''_m} \middle| \sum_l ei \middle| \chi_k \phi_{v_m} \right\rangle \tag{2.29}$$

where, again i stands for the Cartesian coordinates x, y and z. Using 2.26 and 2.24, each term of the sum in 2.28 can be written as:

$$\begin{aligned} \left\langle \chi_r \phi_{v'_m} \middle| ei \middle| \chi_k \phi_{v_m} \right\rangle = {} & \left\langle \chi_r^0 \middle| ei \middle| \chi_k^0 \right\rangle \left\langle \phi_{v'_m}(\boldsymbol{Q_m}) \middle| \phi_{v_m}(\boldsymbol{Q_m}) \right\rangle + \\ & + \sum_t h_{tk}^{\boldsymbol{Q_m}} \left\langle \chi_r^0 \middle| ei \middle| \chi_t^0 \right\rangle \left\langle \phi_{v'_m}(\boldsymbol{Q_m}) \middle| \boldsymbol{Q_m} \middle| \phi_{v_m}(\boldsymbol{Q_m}) \right\rangle + \\ & + \sum_t h_{tr}^{\boldsymbol{Q_m}} \left\langle \chi_k^0 \middle| ei \middle| \chi_t^0 \right\rangle \left\langle \phi_{v_m}(\boldsymbol{Q_m}) \middle| \boldsymbol{Q_m} \middle| \phi_{v'_m}(\boldsymbol{Q_m}) \right\rangle \end{aligned} \tag{2.30}$$

by defining $(\overline{M}_i^0)_{kr} = \left\langle \chi_r^0 \middle| \sum_l ei \middle| \chi_k^0 \right\rangle$ and replacing 2.29 and 2.28 in 2.23 we can finally express the polarizability tensor as:

$$\begin{aligned} (\alpha_{ij})_{k,v_m;n,v'_m} = {} & \frac{1}{h} \sum_r \left[ \frac{(\overline{M}_j^0)_{kr}(\overline{M}_i^0)_{rn}}{\nu_{rk} - \nu_0} + \frac{(\overline{M}_i^0)_{kr}(\overline{M}_j^0)_{rn}}{\nu_{rn} + \nu_0} \right] \left\langle \phi_{v'_m}(\boldsymbol{Q_m}) \middle| \phi_{v_m}(\boldsymbol{Q_m}) \right\rangle + \\ & + \left\langle \phi_{v_m}(\boldsymbol{Q_m}) \middle| \boldsymbol{Q_m} \middle| \phi_{v'_m}(\boldsymbol{Q_m}) \right\rangle \left[ \sum_t \frac{h_{tr}^{\boldsymbol{Q_m}}((\overline{M}_j^0)_{kr}(\overline{M}_i^0)_{nt} + (\overline{M}_i^0)_{rn}(\overline{M}_j^0)_{kt})}{\nu_{rk} - \nu_0} + \right. \\ & \left. + \sum_t \frac{h_{tr}^{\boldsymbol{Q_m}}((\overline{M}_i^0)_{kr}(\overline{M}_j^0)_{nt} + (\overline{M}_j^0)_{rn}(\overline{M}_i^0)_{kt})}{\nu_{rn} + \nu_0} \right] \end{aligned} \tag{2.31}$$

Considering the case where the incident radiation doesn't have enough energy to cause a transition between electronic levels but only between vibrational levels, we would have $k = n$ and $\left\langle \phi_{v'_m}(\boldsymbol{Q_m}) \middle| \phi_{v_m}(\boldsymbol{Q_m}) \right\rangle = 0$ from the orthogonality of the vibrational eigenstates, with the only term left being the second term:

$$\begin{aligned} (\alpha_{ij})_{k,v_m;k,v'_m} = {} & \frac{1}{h} \sum_r \left\langle \phi_{v_m}(\boldsymbol{Q_m}) \middle| \boldsymbol{Q_m} \middle| \phi_{v'_m}(\boldsymbol{Q_m}) \right\rangle \left[ \sum_t \frac{h_{tr}^{\boldsymbol{Q_m}}((\overline{M}_j^0)_{kr}(\overline{M}_i^0)_{nt} + (\overline{M}_i^0)_{rn}(\overline{M}_j^0)_{kt})}{\nu_{rk} - \nu_0} + \right. \\ & \left. + \sum_t \frac{h_{tr}^{\boldsymbol{Q_m}}((\overline{M}_i^0)_{kr}(\overline{M}_j^0)_{nt} + (\overline{M}_j^0)_{rn}(\overline{M}_i^0)_{kt})}{\nu_{rn} + \nu_0} \right] \end{aligned} \tag{2.32}$$

which now depends on the result of the integral: $\langle \phi_{v_m}(\boldsymbol{Q_m}) | \boldsymbol{Q_m} | \phi_{v'_m}(\boldsymbol{Q_m}) \rangle$ and since the $\phi_{v_m}(\boldsymbol{Q_m})$ wave functions have the form of 2.27, from the Hermite polynomials properties it is possible to derive that $(\alpha_{ij})_{k,v_m;k,v'_m}$ can only be non-vanishing if $v'_m = v_m \pm 1$, therefore we arrive at the final conclusion that the only significant Raman lines will arise from the transitions between neighboring vibrational states.

When considering that the system will be at the thermal equilibrium and near room temperature ($\sim$300 K) conditions, we expect that the ground state will be by far the most populated and therefore, transitions from excited initial states ($v_m > 0$) will be much less common, which explains why the stokes Raman lines are more intense that ant-stokes ones.

With those considerations, the only transitions that need to be considered are the ones from the ground state $v_m = 0$ to the first excited state $v'_m = 1$, then the selection rules come from examining the product $\Gamma_{\phi_0} \times \Gamma_{ij} \times \Gamma_{\phi_1}$, which becomes more clear by inspecting the form of the vibrational wave functions (2.28) or more specificaly, the first Hermite polynomials (ARFKEN *et al.*, 2012):

$$\begin{aligned} H_0(x) &= 1 \\ H_1(x) &= 2x \end{aligned} \tag{2.33}$$

Therefore, $\phi_0(\boldsymbol{Q_m})$ will correspond to a totally symmetric irreducible representation, while $\phi_1(\boldsymbol{Q_m})$ will transform according to the symmetry of the mode $\boldsymbol{Q_m}$, which will significantly simplify the selection rules by only requiring the product: $\Gamma_{ij} \times \Gamma_{\phi_1} = \Gamma_{ij} \times \Gamma_{\boldsymbol{Q_m}}$ to contain the totally symmetric representation, which in turn will only happen if $\Gamma_{\boldsymbol{Q_m}} = \Gamma_{ij}$, or in other words, if the vibrational mode $\boldsymbol{Q_m}$ has the same symmetry properties as one of the quadratic products $i \times j = x^2,\ y^2,\ z^2,\ xy,\ xz,\ zy$.

## 2.3 Lattice vibrations and Density Functional Perturbation Theory (DFPT)

As its already established, we will be mainly concerned with the vibrational Raman spectrum, particularly we will be interested in the spectrum generated by the vibrational states of a crystal structure. In order to estimate these modes in a theoretical level, the Density Functional Perturbation Theory (DFPT) can be employed, however in order to contemplate this theoretical framework we must go back to the fundamental problem of solving the Schrödinger equation.

### *2.3.1 Basics of density functional theory*

The main concern of Density Functional Theory (DFT) is with solving the many-body problem in quantum mechanics for a system of interacting electrons and atomic nuclei, based on the foundations from the Hohenberg-Kohn theorem (HOHENBERG; KOHN, 1964), which states that the energy of the ground electronic state is a unique functional of the electron density $n(\boldsymbol{r})$. The procedure is then summarized into solving the Kohn-Sham equations (KOHN; SHAM, 1965):

$$\left[\frac{-\hbar^2\nabla^2}{2m_e} + V_{ei}^{\boldsymbol{R}}(\mathbf{r}) + \frac{e^2}{4\pi\varepsilon_0}\int \frac{n(\mathbf{r'})}{|\mathbf{r}-\mathbf{r'}|}d\mathbf{r'} + V_{xc}(\mathbf{r})\right]\varphi_n(\mathbf{r}) = \varepsilon_n\varphi_n(\mathbf{r}) \tag{2.34}$$

where $V_{ei}^{\boldsymbol{R}}(\mathbf{r})$ is the interaction potential between a static configuration of ions $\boldsymbol{R}$ and the electrons, while $V_{xc}$ is called the exchange-correlation potential and is defined as the functional derivative of the exchange-correlation correction of the energy: $V_{xc} = \frac{\delta\varepsilon_{xc}[n]}{\delta n}$, which accounts for the correction of the errors introduced from the decoupling of the electrons into the independent single-particle Kohn-Sham wave functions $\varphi_n(\mathbf{r})$. Then, the total energy of the fundamental state and the electronic density are given by:

$$E_0 \approx \sum_n \varepsilon_n \tag{2.35}$$

$$n(\mathbf{r}) = \sum_n |\varphi_n(\mathbf{r})|^2 \tag{2.36}$$

The combination of equations 2.34-2.36 can be solved self-consistently, i.e. by using an initial guess for the functions $\varphi_n(\mathbf{r})$, the initial electronic density in 2.36 can be computed and used to estimate the new functions $\varphi_n^{new}(\mathbf{r})$, which can then be used to compute a new electronic density, generating an iterative cycle that continues until the total energy of the ground state in 2.35 is minimized. In principle, these equations can be exactly solved to obtain the ground-state of the system, however in practice the exchange-correlation functional $\varepsilon_{xc}[n]$ is not known exactly. The success of DFT comes from the fact that $\varepsilon_{xc}[n]$ can be estimated with simple enough approximations, among those, some of the most famous ones include the Local Density Approximation (LDA) (CEPERLEY; ALDER, 1980), which considers the parametrizations of a homogeneous interacting electron gas and the Generalized-Gradient Approximations (GGA), derived initially from the Pardew-Burke-Ernzerhof (PBE) (PERDEW *et al.*, 1996b) approximation,

which in addition to LDA, introduces a dependence of $\varepsilon_{xc}[n]$ on the local gradient of the electron density to better account for inhomogeneous density distributions (HEID, 2013).

### *2.3.2 Lattice dynamics*

DFT is mainly concerned with the electron system, however, we will be interested in how these electrons will impact on the vibrations of a crystal lattice. In order to evaluate this interaction, we must resort again to the Born-Oppenheimer approximation and decouple the two systems, however this time, the main concern will be the effective potential felt by the atomic lattice (HEID, 2013):

$$V(\boldsymbol{R}) = V_{ii}(\boldsymbol{R}) + E_0(\boldsymbol{R}) \tag{2.37}$$

where $\boldsymbol{R}$ represents the set of all positions of the ions in the lattice, $V_{ii}$ is the term containing the ion-ion interactions, while $E_0(\boldsymbol{R})$ represents the ground-state energy of the electrons for a given set of ionic positions $\boldsymbol{R}$, which can be estimated from equation 2.35 by solving the Kohn-Sham equations.

If we consider the limit of small displacements around the equilibrium positions: $\boldsymbol{R} = \boldsymbol{R^0} + \boldsymbol{u}$, then the effective potential can be expanded as:

$$V(\boldsymbol{R}) = \frac{1}{2} \sum_{\alpha,i;\beta,j} (\Phi_{\alpha i;\beta j}) u_{\alpha i} u_{\beta j} \tag{2.38}$$

where $\Phi_{\alpha i;\beta j}$ are the set of atomic force constants between atoms $\alpha$ and $\beta$, with $i$ and $j$ representing the Cartesian directions. Here, the zeroth-order term $V(\boldsymbol{R^0})$ was chosen as the reference value for the potential, the first-order term vanishes in the equilibrium configuration $\boldsymbol{R^0}$ and the second-order term represents the harmonic approximation, with the harmonic interatomic force constants given by:

$$\Phi_{\alpha i;\beta j} = \frac{\partial^2 V}{\partial R_{\alpha i} \partial R_{\beta j}} \tag{2.39}$$

When considering a crystal lattice, each atom has to be characterized by two indices: $\alpha = (a,k)$, with $a$ denoting the unit cell index $k$ the index of the atom inside a unit cell such that: $u_{\alpha i} = u^a_{ki}$. The problem then turns to the solution of the set of Newtonian equations of motion:

$$m_k \frac{d^2 u_{ki}^a}{dt^2} = -\sum_{b,k',j} (\Phi_{ki;k'j}^{a;b}) u_{k'j}^b \tag{2.40}$$

when considering periodic boundary conditions, the solution of 2.40 becomes:

$$u_{ki}^a = \frac{1}{\sqrt{m_k}} \eta_{ki}(n\boldsymbol{q}) e^{i\boldsymbol{q}\cdot\boldsymbol{R}_{\boldsymbol{k}}^{0a}} e^{-i\omega(n\boldsymbol{q})t} \tag{2.41}$$

with $R_k^{0a}$ as the equilibrium position of the k-th atom in the a-th unit cell. Replacing this solution into 2.40 results in:

$$\omega^2(n\boldsymbol{q})\eta_{ki}(n\boldsymbol{q}) = \sum_{k'j} D_{ki;k'j}(\boldsymbol{q})\eta_{k'j}(n\boldsymbol{q}) \tag{2.42}$$

and the solutions come from the diagonalization of the dynamical matrix:

$$D_{ki;k'j}(\boldsymbol{q}) = \frac{1}{\sqrt{m_k m_{k'}}} \sum_b (\Phi_{ki;k'j}^{a;b}) e^{i\boldsymbol{q}\cdot(R_{k'}^{0b} - R_k^{0a})} \tag{2.43}$$

and the result will be the set of eigenvectors $\eta_{ki}(n\boldsymbol{q})$ and frequencies $\omega(n\boldsymbol{q})$ that will correspond to the phonon displacements and frequencies.

### *2.3.3 The linear response formulation*

The procedure outlined above is only possible if the interatomic force constants (2.39) are known and that requires the knowledge of second-order derivatives of the energy of the system. In the approximations utilized here, the lattice dynamics depends only on ground-state properties of the electronic system and its derivatives, which can be obtained in the framework of density functional theory by using perturbative schemes, hence the name of the method: Density functional Perturbation Theory.

In contrast to the procedure of 2.37, we now consider the coupled interactions between electrons and ions as an external potential $V_{ei}^{\boldsymbol{R}}(\mathbf{r})$, such that the potential felt by the ions becomes:

$$V(\boldsymbol{r},\boldsymbol{R}) = V_{ii}(\boldsymbol{R}) + V_{ei}^{\boldsymbol{R}}(\mathbf{r}) \tag{2.44}$$

Using the Hellmann–Feynman theorem, the first-order derivative of the potential given in 2.37 can be expressed as (GIANNOZZI; BARONI, 2005):

$$\frac{\partial V}{\partial R_{\alpha i}} = \langle \varphi(\boldsymbol{R}) | \frac{\partial H}{\partial R_{\alpha i}} | \varphi(\boldsymbol{R}) \rangle = \int n(\boldsymbol{r}) \frac{\partial V_{ei}^{\boldsymbol{R}}(\mathbf{r})}{\partial R_{\alpha i}} d\boldsymbol{r} + \frac{\partial V_{ii}(\boldsymbol{R})}{\partial R_{\alpha i}} \tag{2.45}$$

The second-order derivative can then be obtained as:

$$\frac{\partial^2 V}{\partial R_{\alpha i} \partial R_{\beta j}} = \int \frac{\partial n(\boldsymbol{r})}{\partial R_{\beta j}} \frac{\partial V_{ei}^{\boldsymbol{R}}(\mathbf{r})}{\partial R_{\alpha i}} d\boldsymbol{r} + \delta_{\alpha\beta} \int n(\boldsymbol{r}) \frac{\partial^2 V_{ei}^{\boldsymbol{R}}(\mathbf{r})}{\partial R_{\alpha i} \partial R_{\beta j}} d\boldsymbol{r} + \frac{\partial^2 V_{ii}(\boldsymbol{R})}{\partial R_{\alpha i} \partial R_{\beta j}} \tag{2.46}$$

In this way, the calculation of the interatomic force constants mainly becomes the task of finding both ground-state electronic density $n(\boldsymbol{r})$ as well as its linear response to a displacement in the atomic positions $\frac{\partial n(\boldsymbol{r})}{\partial \boldsymbol{R}}$. The first can be found from the regular DFT self-consistent procedure, while the latter can derived by applying the derivative to the equation 2.36 as:

$$\frac{\partial n(\boldsymbol{r})}{\partial R_{\alpha i}} = 2Re \left\{ \sum \varphi_n^*(\mathbf{r}) \frac{\partial \varphi_n(\mathbf{r})}{\partial R_{\alpha i}} \right\} \tag{2.47}$$

And the first-order derivative (linear response) of the Kohn-Sham states can be obtained from equation 2.34 as (GIANNOZZI; BARONI, 2005):

$$(H_{SCF} - \varepsilon_n) \frac{\partial \varphi_n(\boldsymbol{r})}{\partial R_{\alpha i}} = - \left( \frac{\partial V_{SCF}(\boldsymbol{r})}{\partial R_{\alpha i}} - \frac{\partial \varepsilon_n}{\partial R_{\alpha i}} \right) \varphi_n(\boldsymbol{r}) \tag{2.48}$$

where:

$$V_{SCF} = V_{ei}^{\boldsymbol{R}}(\mathbf{r}) + \frac{e^2}{4\pi\varepsilon_0} \int \frac{n(\mathbf{r'})}{|\mathbf{r} - \mathbf{r'}|} d\mathbf{r'} + V_{xc}(\mathbf{r}) \tag{2.49}$$

$$H_{SCF} = -\frac{\hbar^2}{2m_e} \frac{\partial^2}{\partial \boldsymbol{r}^2} + V_{SCF} \tag{2.50}$$

and:

$$\frac{\partial V_{SCF}(\boldsymbol{r})}{\partial R_{\alpha i}} = \frac{\partial V_{ei}^{\boldsymbol{R}}(\mathbf{r})}{\partial R_{\alpha i}} + \frac{e^2}{4\pi\varepsilon_0} \int \frac{1}{|\mathbf{r} - \mathbf{r'}|} \frac{\partial n(\mathbf{r'})}{\partial R_{\alpha i}} d\mathbf{r'} + \int \frac{\delta V_{xc}(\mathbf{r})}{\delta n(\boldsymbol{r'})} \frac{\partial n(\boldsymbol{r'})}{\partial R_{\alpha i}} d\boldsymbol{r'} \tag{2.51}$$

$$\frac{\partial \varepsilon_n}{\partial R_{\alpha i}} = \langle \varphi_n | \frac{\partial V_{SCF}}{\partial R_{\alpha i}} | \varphi_n \rangle \tag{2.52}$$

Equations 2.47–2.52 form another set of self-consistent linear equations. Based on the regular DFT electronic density and on an initial guess for the linear responses of the wave functions $\frac{\partial \varphi_n(\boldsymbol{r})}{\partial R_{\alpha i}}$, we can use an iterative process to refine the linear responses until self-consistency is achieved and the derivatives in 2.46 can be calculated to finally construct and diagonalize the dynamical matrix (2.43).

# 3 MATERIALS AND METHODS

## 3.1 Material Synthesis

**$[(CH_3)_2NH_2]_2SnBr_6$**: The compound was grown by the slow evaporation method dissolving 1 mmol of $SnBr_2$ in N, N-dimethylformamide (DMF), adding an aqueous solution of HBr at 90 ºC. The resulting solution was stirred and then kept at room temperature. After 2 weeks, gradual evaporation of the solution led to the growth of high-quality, transparent crystals exhibiting a bright-yellow coloration in the form of bars. The reagents used in synthesizing were from commercial sources purchased from Sigma Aldrich and Alfa Aesar.

## 3.2 Differential Scanning Calorimetry (DSC)

The thermal analysis was performed on a Netzsch Maia 200 F3. Measurements were obtained from several cooling and heating cycles in different temperatures; the used rates were 5 K/min from 200K to 140K. In a typical measurement, in which all the sensors and crucibles were kept under a constant flow of nitrogen during the experiment, 10 mg of sample were deposited in a pierced aluminum pan and analyzed with the same conditions as the reference one pierced aluminum pan.

## 3.3 Single-Crystal x-ray diffraction (XRD)

Single crystal X-ray diffraction data ($\phi$ scans and $\omega$ scans with $\kappa$ and $\theta$ offsets) were collected on a Bruker D8 Venture $\kappa$-geometry diffractometer equipped with a Photon II CPAD detector and an I$\mu$S 3.0 Incoatec Mo K$\alpha$ ($\lambda$ = 0.71073 Å) microfocus source. Suitable crystals from each sample were harvested and mounted on MiTeGen MicroMount using immersion oil. The APEX 4 software was used for the unit cell determination and data collection. The data reduction and global cell refinement were made using the Bruker SAINT+ software package, and a multi-scan absorption correction was performed with SADABS (KRAUSE *et al.*, 2015). Using the Olex2 (DOLOMANOV *et al.*, 2009) interface program to the SHELX suite (SHELDRICK, 2008), the structure was solved by the intrinsic phasing method implemented in ShelXT (SHELDRICK, 2015), allowing the location of most of the atoms. The remaining atoms were located from different Fourier maps calculated from successive full-matrix least-squares refinement cycles on F2 with ShelXL and refined using anisotropic displacement parameters.

MERCURY (MACRAE *et al.*, 2020) and VESTA (MOMMA; IZUMI, 2011) were used to prepare the artwork representations for publication.

## 3.4 Raman Spectroscopy

The low-temperature Raman active dependence spectra, from 10 K until room temperature, were collected using a T64000 Jobin–Yvon spectrometer equipped with an Olympus microscope and an LN2-cooled CCD to detect the scattered light. The spectra were excited with an Argon ion laser ($\lambda$ = 514.5 nm). The spectrometer slits were set to give a spectral resolution better than 2 $cm^{-1}$. All measurements were performed using a long working distance plan-achromatic objective (20.00×0.35×20.50 mm). The temperature-dependent spectra were obtained by keeping the sample in a vacuum inside a He-compressed closed-cycle cryostat. A Lakeshore 330 controller controlled the temperature, keeping the precision around 1 K. Each Raman spectrum was deconvoluted in the sum of Lorentzian functions, using the Fityk software (WOJDYR, 2010).

## 3.5 Computational Methods

In this work, the calculations were performed under the aproximations of the density functional theory (DFT) implemented in the Quantum-ESPRESSO package (GIANNOZZI *et al.*, 2009; GIANNOZZI *et al.*, 2017). A structural optimization was initially performed using a 6 x 6 x 3 Monkhorst-Pack grid and a 65 Ry kinetic energy cutoff for wavefunctions followed by the Γ-point phonon calculations, which used 8 x 8 x 4 grid and a 80 Ry cutoff. All calculations were done using the SG15 Optimized Norm-Conserving Vanderbilt pseudopotentials (HAMANN, 2013). The the phonon frequencies were calculated within the density functional perturbation theory (DFPT) using an exchange-correlation term determined within the generalized gradient approximation (GGA) parameterized by Perdev–Burke–Ernzerhof (PBE) (PERDEW *et al.*, 1996a). All calculations present in this work were performed using the computational resources of the "Centro Nacional de Processamento de Alto Desempenho em São Paulo (CENAPAD-SP)."

# 4 RESULTS AND DISCUSSIONS

## 4.1 Structural Details

Through Single-Crystal X-Ray Diffraction (SCXRD) measurements it was found that, at room temperature, $(DMA)_2SnBr_6$ crystallizes in the orthorhombic Pnmn space group. In this structure, the $Sn^{4+}$ cations are centered inside the isolated $[SnBr_6]^{2-}$ octahedra that form a zero-dimensional vacancy-ordered double perovskite structure ($A_2BX_6$) with the A site being occupied by the $DMA^+$ cations (see Figure 5). Upon cooling the sample, two other phases were found: a monoclinic phase with P2/m space group at 160 K and a triclinic phase with $P\bar{1}$ space group at 100 K. Figure 5 displays the unit cell at each different phase and Table 1 provides the crystallographic data for each temperature where SCXRD measurements were performed.

Figure 5 – Unit cell of $(DMA)_2SnBr_6$ at the temperatures of: 300K, 160K and 100K.

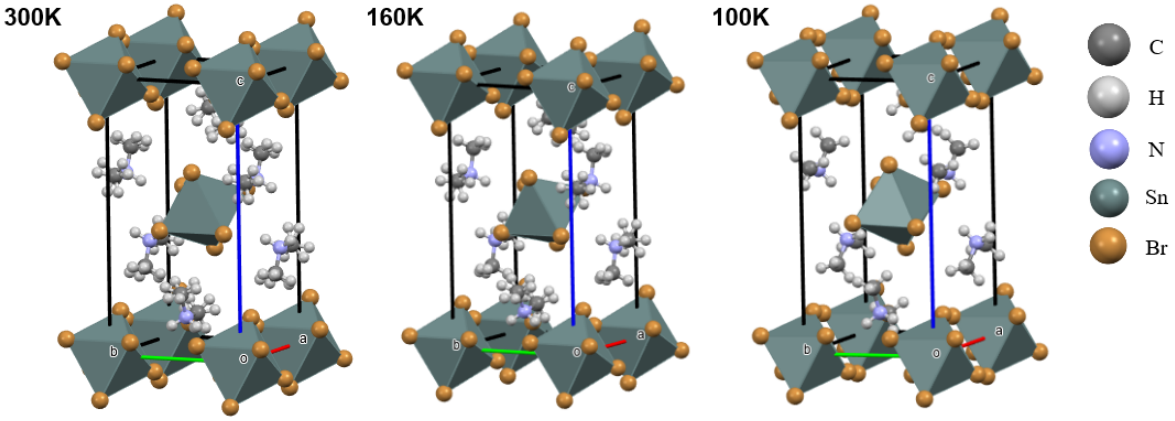

Table 1 – Crystal data and refinement parameters of $[(CH_3)_2NH_2)]_2SnBr_6$ at different temperature conditions.

| Chemical Formula | $[(CH_3)_2NH_2)]_2SnBr_6$ | | | | | | | |
|---|---|---|---|---|---|---|---|---|
| Temperature (K) | 300 | 280 | 250 | 230 | 200 | 160 | 130 | 100 |
| Space Group | Pnmn | | | | | P2/m | | $P\bar{1}$ |
| Unit cell Dimensions | | | | | | | | |
| a (Å) | 7.5967(14) | 7.5830(5) | 7.5698(4) | 7.5554(6) | 7.5396(8) | 7.5215(8) | 7.5157(9) | 7.5021(7) |
| b (Å) | 7.5782(13) | 7.5590(4) | 7.5443(3) | 7.5346(4) | 7.5229(6) | 7.5062(6) | 7.4964(7) | 7.4904(6) |
| c (Å) | 14.848(3) | 14.8061(9) | 14.7914(7) | 14.7735(11) | 14.7564(15) | 14.7314(15) | 14.7010(17) | 14.6591(12) |
| $\alpha$ | 90 | 90 | 90 | 90 | 90 | 90 | 90 | 88.520(3) |
| $\beta$ | 90 | 90 | 90 | 90 | 90 | 90.336(4) | 90.426(5) | 88.885(2) |
| $\gamma$ | 90 | 90 | 90 | 90 | 90 | 90 | 90 | 88.049(2) |
| Volume ($Å^3$) | 854.8(3) | 848.68(9) | 844.72(7) | 841.01(10) | 836.98(14) | 831.69(14) | 828.24(16) | 822.86(12) |
| Density ($mg/m^3$) | 2.682 | 2.701 | 2.714 | 2.726 | 2.739 | 2.757 | 2.768 | 2.786 |
| $\mu$ ($mm^{-1}$) | 28.105 | 15.602 | 15.675 | 15.744 | 15.820 | 15.921 | 15.987 | 16.092 |
| F/000 | 628 | | | | | | | |
| Z | 2 | | | | | | | |
| Radiation | MoK$\alpha$ ($\lambda$ = 0.71073) | | | | | | | |
| $2\theta$ range for data collection | 5.960 to 70.292 | 2.752 to 28.262 | 2.75 to 28.99 | 2.757 to 28.111 | 2.761 to 28.433 | 1.382 to 30.758 | 1.385 to 30.742 | 2.717 to 30.590 |
| Reflections collected | 8825 | 10093 | 33445 | 26838 | 25461 | 39272 | 37814 | 5056 |
| Crystal Size ($mm^3$) | 0.378 x 0.22 x 0.098 | | | | | | | |
| Index ranges | $-8 \leq h \leq 9$, $-18 \leq k \leq 18$, $-9 \leq l \leq 9$ | $-10 \leq h \leq 10$, $-19 \leq k \leq 16$, $-9 \leq l \leq 10$ | $-10 \leq h \leq 10$, $-19 \leq k \leq 19$, $-10 \leq l \leq 10$ | $-10 \leq h \leq 10$, $-19 \leq k \leq 19$, $-10 \leq l \leq 10$ | $-10 \leq h \leq 10$, $-19 \leq k \leq 19$, $-10 \leq l \leq 10$ | $-10 \leq h \leq 10$, $-10 \leq k \leq 10$, $-21 \leq l \leq -21$ | $-10 \leq h \leq 10$, $-10 \leq k \leq 10$, $-21 \leq l \leq -21$ | $-10 \leq h \leq 10$, $-10 \leq k \leq 10$, $-21 \leq l \leq -21$ |
| Goodness-of-fit on F2 | 1.063 | 1.164 | 1.258 | 1.223 | 1.260 | 1.161 | 1.193 | 1.071 |
| Final R indexes | R1 = 0.0433 | R1 = 0.0309 | R1 = 0.0398 | R1 = 0.0625 | R1 = 0.1034 | R1 = 0.0367 | R1 = 0.0394 | R1 = 0.0889 |
| [$I \geq 2\sigma$ (I)] | wR2 = 0.1180 | wR2 = 0.0524 | wR2 = 0.0896 | wR2 = 0.1498 | wR2 = 0.2646 | wR2 = 0.0681 | wR2 = 0.0744 | wR2 = 0.2626 |
| Final R indexes | R1 = 0.0469 | R1 = 0.0442 | R1 = 0.0440 | R1 = 0.0676 | R1 = 0.1077 | R1 = 0.0455 | R1 = 0.0458 | R1 = 0.1018 |
| [all data] | wR2 = 0.1220 | wR2 = 0.0574 | wR2 = 0.0914 | wR2 = 0.1520 | wR2 = 0.2660 | wR2 = 0.0727 | wR2 = 0.0772 | wR2 = 0.2746 |

Figures 6 a), b) and c) show the temperature-dependent behavior of the lattice parameters and the cell volume. From the a and b lattice parameters, we can identify two different behaviors before and after 200 K, while the c lattice parameter shows a discontinuous decrease around 280 K.

Figure 6 – (a) lattice parameters a and b vs T, (b) lattice parameter c vs T and (c) unit cell volume vs T

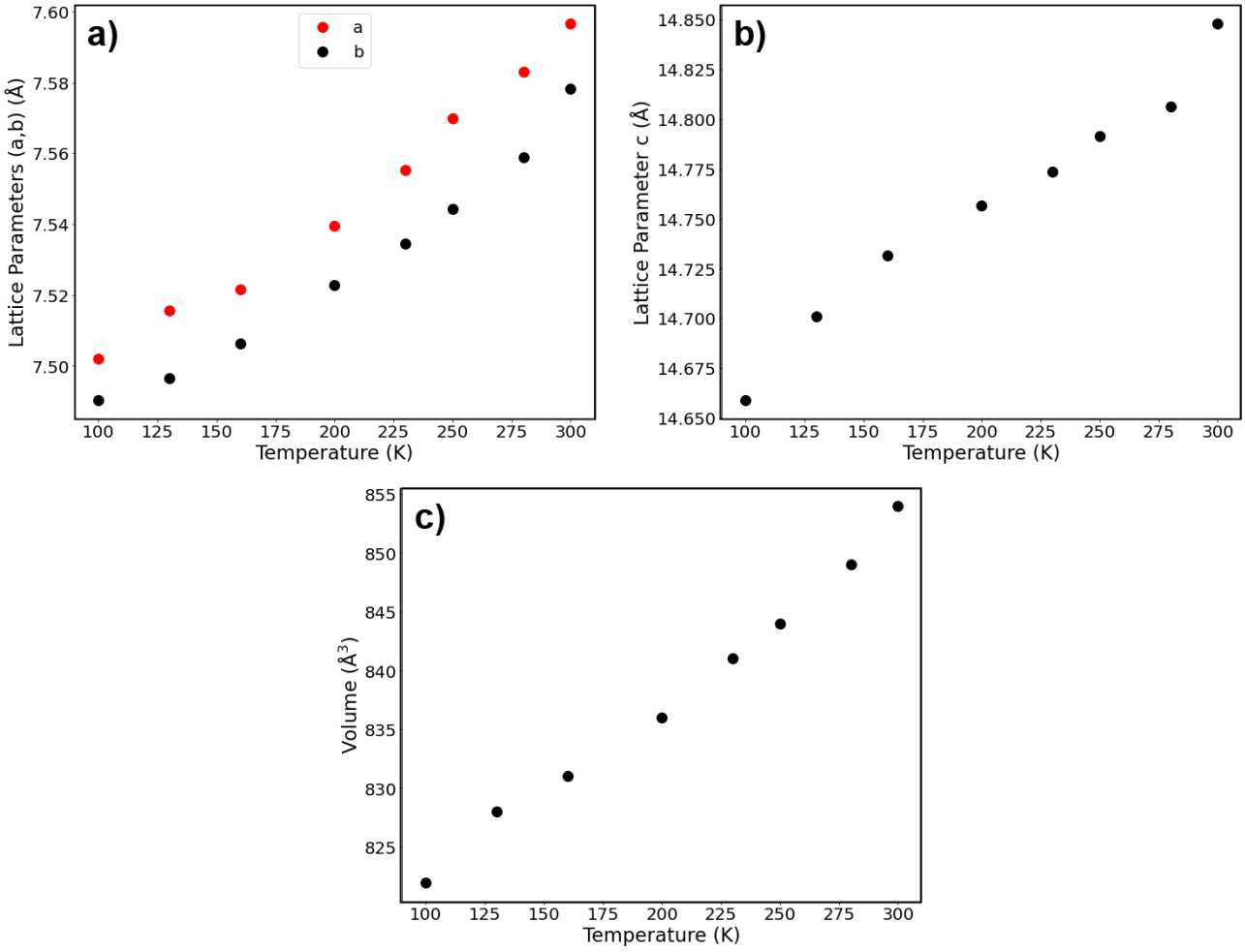


The SCXRD results are also supported by DSC analysis (see Figure 7) through the presence of a heat anomaly with onsets at about 190 K and 200 K on the heating and cooling run respectively. However, at least three other heat events/anomalies also appear close to 220 K, 260 K and 270 K.

The $[SnBr_6]^{2-}$ octahedra are found to be distorted relative to the octahedra in the classic cubic perovskite structures. The Sn-Br bond lengths are found in the range between 2.6056(12) Å and 2.5825(15) Å across all the three phases. At both the orthorhombic (300 K) and the monoclinic (160 K) phases, $[SnBr_6]^{2-}$ ions are found in a $C_{2h}$ site and two independent

Figure 7 – DSC traces for $(DMA)_2SnBr_6$ between 160 K and 280 K showing both the cooling and the heating run

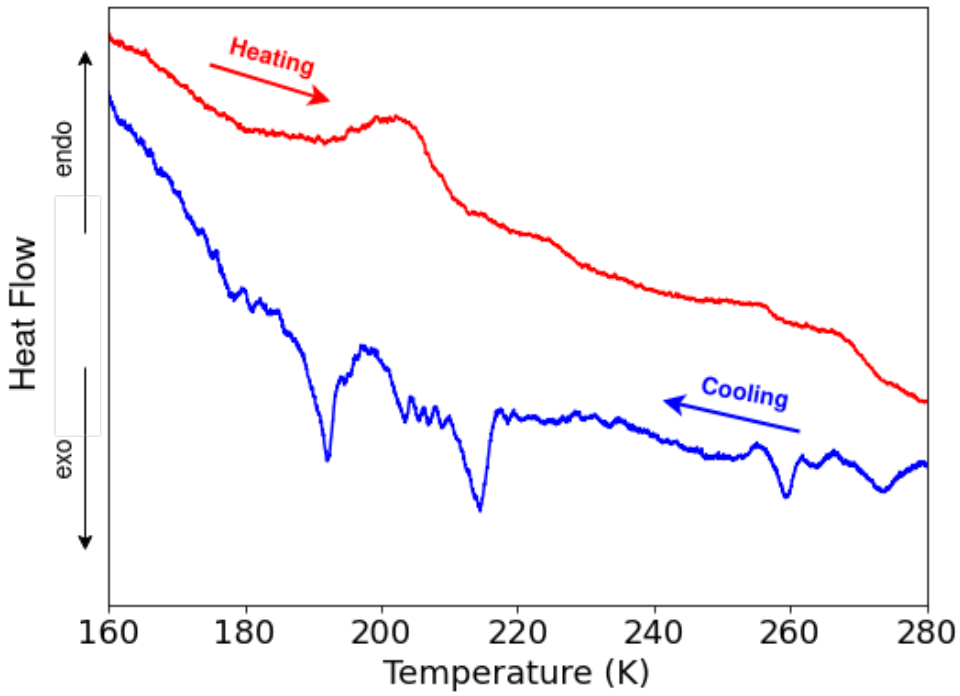


Sn-Br bond lengths are found for each symmetry-independent octahedron while, at the triclinic phase, the octahedra are found in lower symmetry $C_i$ sites and the two symmetry-independent octahedra have three independent Sn-Br bond lengths. The Br-Sn-Br angles also differ slightly from the 90° octahedral angles and to better represent both the angle distortion ($\sigma$) and the length distortion ($\Delta d$) we use the following expressions:

$$\Delta d = \left(\frac{1}{6}\right)\sum\left(\frac{d_n - d}{d}\right)^2 \tag{4.1}$$

$$\sigma = \left(\frac{1}{12}\right)\sum\left(\frac{\theta_n - 90}{90}\right)^2 \tag{4.2}$$

Where $d$ is the average Sn-Br bond length of the octahedron, while $d_n$ and $\theta_n$ represent the nth Sn-Br bond length and Br-Sn-Br angle respectively.

The temperature dependence of the calculated distortions are displayed in Figure 8, which immediately shows how both of these quantities suffer discontinuities during the phase transitions, with the bond length distortions suffering an increase while the angular distortions suffers an overall reduction at the lower temperatures. Another feature that is important to point out is the discontinuous reduction of the angular distortion that appears at 280 K, which could be

Figure 8 – (a) Bond length and angle distortions for each symmetry independent octahedron (b) Symmetry-independent cations ($DMA^+$ and $[SnBr_6]^{2-}$) inside the unit cell at the orthorhombic (O), monoclinic (M) and triclinic (T) phases.

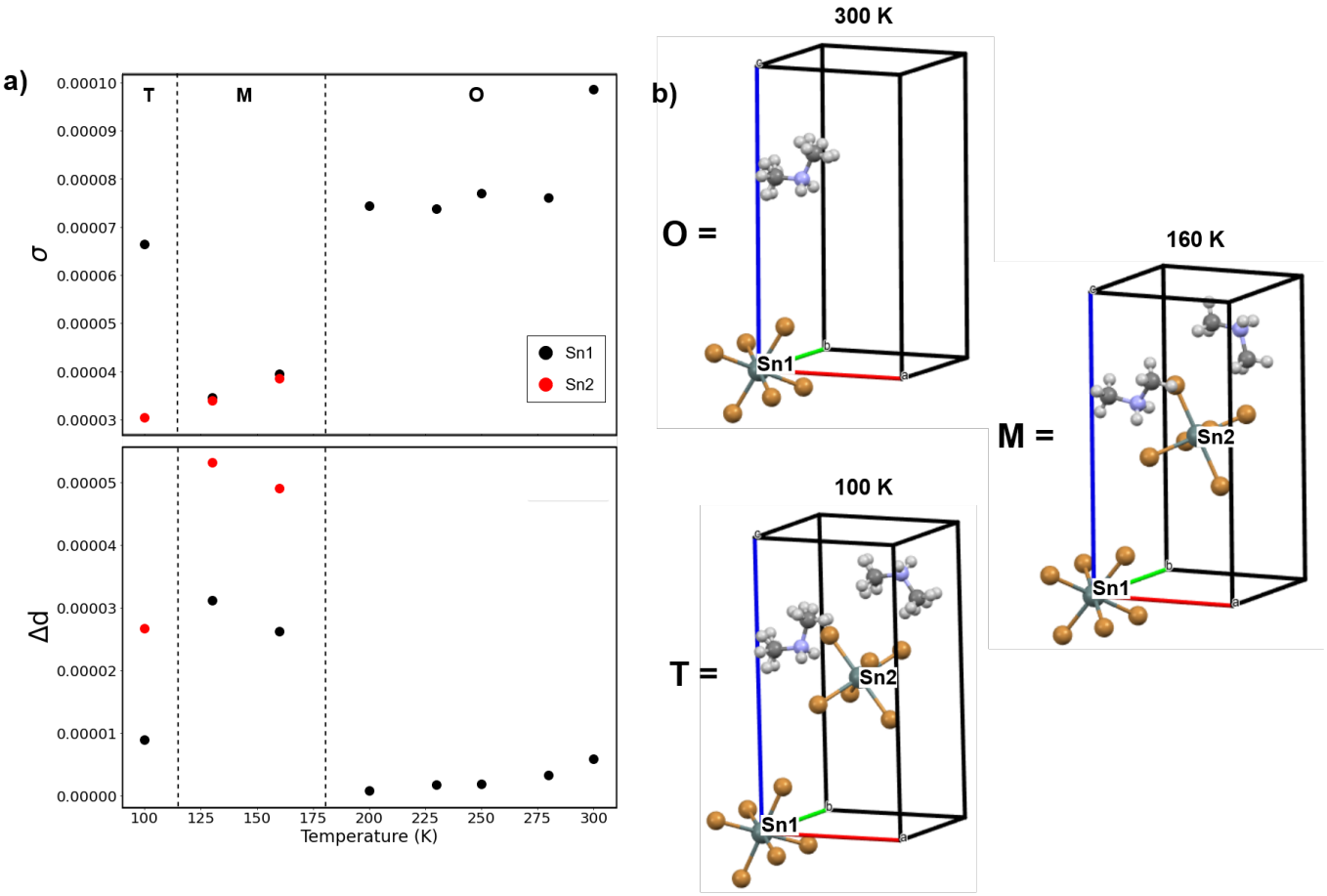


another evidence for the previously mentioned event that is observed for the lattice parameter c and also could be related to one of the heat anomalies observed in the DSC trace at the higher temperatures.

The hydrogens of the $NH_2$ group of the $DMA^+$ cation have well defined positions in all phases, with the N-H bond length only increasing slightly from 0.890 Å at the orthorhombic phase to 0.910 Å at the monoclinic phase and ranging from 0.906 Å to 0.912 Å at the triclinic phase. The H-N-H angle also varies by a very small amount, ranging from 107.39° to 107.32° across all phases. This protonic ordering effect can be attributed to the formation of hydrogen bonds with the Br atoms from the $[SnBr_6]^{2-}$ octahedra (see Figure 9) which are also expected to largely contribute to the overall crystal lattice stability (EL-MELLOUHI *et al.*, 2016), however, the relative weakness of these bonds is what could enable the highly dynamic behavior of the DMA molecules inside the structure.

Meanwhile, the hydrogens of the $CH_3$ groups are shown to be disordered both in the

Figure 9 – Hydrogen bonds between the $NH_2$ group of the $DMA^+$ cation and the $[SnBr6]^{2-}$ octahedrons

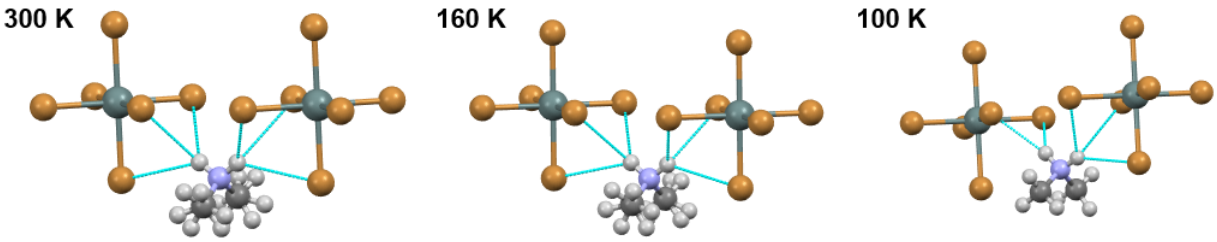


orthorhombic phase (300 K) and in the monoclinic phase (160 K) and furthermore, both of these phases only differ by small atomic displacements, indicating that this first phase transition has a displacive nature, however in the triclinic phase (100 K) the disorder disappears, indicating that the second phase transition has an order-disorder nature.

## 4.2 Symmetry mode analysis

Since it was already possible to identify the nature of the observed phase transitions, before proceeding to the analysis of the vibrational Raman spectra, we can use symmetry considerations to comprehend some of the mechanisms that are involved in the observed events. Here, the focus will be given to the displacive phase transition, since its more straight forward to relate the high symmetry phase to the low symmetry one. Furthermore, the initial objective is to gain insight into the observed structural distortions in a way that allows to relate them to the vibrational modes that will be later analyzed in the Raman spectrum.

Generally, the lattice modes that drive the symmetry break during a displacive phase transition transform according to a single irreducible representation (irrep) of the crystal's point group, which is known as the active irrep of the phase transition (PEREZ-MATO *et al.*, 2010). Since the structure under study can be thought as an ordered arrangement of two very distinct components: the organic $DMA^+$ cation and the inorganic $[SnBr_6]^{2-}$ anion, being somewhat weakly coupled due to their opposite excess charges and the formation of hydrogen bonds, it becomes necessary to analyze them separately, meaning that the separate degrees of freedom and symmetries of each component will need to be linked to the degrees of freedom and the point group of the crystal. Hence a factor group analysis was carried out and the irreps of each the internal modes from the ionic components ($DMA^+$ and $[SnBr_6]^{2-}$) have been correlated to the irreps of $(DMA)_2SnBr_6$ point group ($D_{2h}$) as is displayed in Table 2.

Table 2 – Correlation diagram between the irreps of the free ions and the irreps of the $(DMA)_2SnBr_6$ point group

| Ion | Vibration | Free ion symmetry | Site symmetry | Factor group symmetry |
|---|---|---|---|---|
| $DMA^+$ | | $C_{2v}$ ($C_2$(z)) | $C_s$ ($\sigma$(zx)) | $D_{2h}$ |
| | $\nu_s(NH_2)$ | $A_1$ | A' | $A_g + B_{2g} + B_{1u} + B_{3u}$ |
| | $\nu_{as}(NH_2)$ | $B_2$ | A" | $B_{1g} + B_{3g} + A_u + B_{2u}$ |
| | $\delta(NH_2)$ | $A_1$ | A' | $A_g + B_{2g} + B_{1u} + B_{3u}$ |
| | $\rho(NH_2)$ | $B_2$ | A" | $B_{1g} + B_{3g} + A_u + B_{2u}$ |
| | $\omega(NH_2)$ | $B_1$ | A' | $A_g + B_{2g} + B_{1u} + B_{3u}$ |
| | $\tau(NH_2)$ | $A_2$ | A" | $B_{1g} + B_{3g} + A_u + B_{2u}$ |
| | $\nu_s$(CNC) | $A_1$ | A' | $A_g + B_{2g} + B_{1u} + B_{3u}$ |
| | $\nu_{as}$(CNC) | $B_1$ | A' | $A_g + B_{2g} + B_{1u} + B_{3u}$ |
| | $\delta$(CNC) | $A_1$ | A' | $A_g + B_{2g} + B_{1u} + B_{3u}$ |
| | $\nu_s(CH_3)$ | $A_1 + B_1$ | 2A' | $2A_g + 2B_{2g} + 2B_{1u} + 2B_{3u}$ |
| | $\nu_{as}(CH_3)$ | $A_1 + B_1 + B_2 + A_2$ | 2A' + 2A" | $2A_g + 2B_{1g} + 2B_{2g} + 2B_{3g}$ $+2A_u + 2B_{1u} + 2B_{2u} + 2B_{3u}$ |
| | $\delta_s(CH_3)$ | $A_1 + B_1$ | 2A' | $2A_g + 2B_{2g} + 2B_{1u} + 2B_{3u}$ |
| | $\delta_{as}(CH_3)$ | $A_1 + B_1 + B_2 + A_2$ | 2A' + 2A" | $2A_g + 2B_{1g} + 2B_{2g} + 2B_{3g}$ $+2A_u + 2B_{1u} + 2B_{2u} + 2B_{3u}$ |
| | $\rho(CH_3)$ | $A_1 + B_1 + B_2 + A_2$ | 2A' + 2A" | $2A_g + 2B_{1g} + 2B_{2g} + 2B_{3g}$ $+2A_u + 2B_{1u} + 2B_{2u} + 2B_{3u}$ |
| | $\tau(CH_3)$ | $A_2 + B_2$ | 2A" | $2B_{1g} + 2B_{3g} + 2A_u + 2B_{2u}$ |
| | L | $A_2 + B_1 + B_2$ | A' + 2A" | $A_g + 2B_{1g} + B_{2g} + 2B_{3g}$ $+2A_u + B_{1u} + 2B_{2u} + B_{3u}$ |
| | T | $A_1 + B_1 + B_2$ | 2A' + A" | $2A_g + B_{1g} + 2B_{2g} + B_{3g}$ $+A_u + 2B_{1u} + B_{2u} + 2B_{3u}$ |
| $[SnBr_6]^{2-}$ | | $O_h$ | $C_{2h}$ ($C_2$(y)) | $D_{2h}$ |
| | $\nu_1$ | $A_{1g}$ | $A_g$ | $A_g + B_{2g}$ |
| | $\nu_2$ | $E_g$ | $A_g + B_g$ | $A_g + B_{1g} + B_{2g} + B_{3g}$ |
| | $\nu_3$ | $T_{1u}$ | $A_u + 2B_u$ | $A_u + 2B_{1u} + B_{2u} + 2B_{3u}$ |
| | $\nu_4$ | $T_{1u}$ | $A_u + 2B_u$ | $A_u + 2B_{1u} + B_{2u} + 2B_{3u}$ |
| | $\nu_5$ | $T_{2g}$ | $2A_g + B_g$ | $2A_g + B_{1g} + 2B_{2g} + B_{3g}$ |
| | $\nu_6$ | $T_{2u}$ | $2A_u + B_u$ | $2A_u + B_{1u} + 2B_{2u} + B_{3u}$ |
| | L | $T_{1g}$ | $A_g + 2B_g$ | $A_g + 2B_{1g} + B_{2g} + 2B_{3g}$ |
| | T | $T_{1u}$ | $A_u + 2B_u$ | $A_u + 2B_{1u} + B_{2u} + 2B_{3u}$ |

The free $DMA^+$ cation has $C_{2v}$ symmetry and 30 internal modes (including librations) which are distributed among the irreducible representations as: $\Gamma_{DMA} = 9A_1 + 6A_2 + 8B_1 + 7B_2$. In an ideal cubic perovskite structure the $[SnBr_6]^{2-}$ octahedron would have $O_h$

symmetry and 7 internal modes (also including librations) that can be distributed as: $\Gamma_{oct}$ = $A_{1g}$ + $E_g$ + $T_{2u}$ + $T_{2g}$ + $2T_{1u}$ + $T_{1g}$. In this way, all degrees of freedom have been accounted and from the factor-group splitting they become the total of 174 modes of the complete mechanical representation $\Gamma = 24A_g + 18B_{1g} + 24B_{2g} + 18B_{3g} + 19A_u + 26B_{1u} + 19B_{2u} + 26B_u$.

To find the active irrep of the displacive phase transition, the AMPLIMODES tool on the Bilbao Crystallographic Server (OROBENGOA *et al.*, 2009) was employed using the structures at 300 K and 160 K without the disordered hydrogens as inputs. To summarize short, the program initially transforms the high-symmetry structure to the basis of the low-symmetry phase and then maps the atoms in the actual low symmetry phase to the atoms on this new transformed (high-symmetry) structure. After this mapping, the set of displacement vectors for each atom $\boldsymbol{u_k}$ can be calculated and expressed in a basis symmetry-adapted distortion modes: $\boldsymbol{u_k} = \sum_j A_{jk}\boldsymbol{\epsilon}_{jk}$, where the symmetry properties of a mode $\boldsymbol{\epsilon_j}$ are characterized by an irrep of the high-symmetry space group G, defining its transformation properties under the operations of this group. Finally, the program will output the set of $\boldsymbol{\epsilon_j}$ modes and a total amplitude $A_j = \left[\sum (A_{jk})^2\right]^{\frac{1}{2}}$ for each irrep involved in the phase transition.

The obtained results (see Table 3 and Figure 10) show that the displacements of the atoms can be described by two vector basis sets: one that transforms according to the $A_{1g}$ irrep, that is not responsible for any symmetry reduction, and one that transforms according to $B_{2g}$ that reduces the symmetry to P2/m and as expected for the active irrep, has a higher amplitude and therefore represents most of the structural distortion.

Table 3 – Summary of AMPLIMODES output

| K-point | Irrep | Isotropy Subgroup | Basis Dimension | Amplitude (Å) |
|---|---|---|---|---|
| Γ | $A_{1g}$ | Pnnm | 14 | 0.1917 |
| Γ | $B_{2g}$ | P2/m | 14 | 1.0330 |

Knowing that $B_{2g}$ is the active irrep and from inspecting Table 2, we can find all the internal modes that could possibly be directly involved/affected by the phase transition. For $DMA^+$, these include: a librational mode (L), all types of the C-N-C skeleton vibrations ($\nu_s$(CNC), $\nu_{as}$(CNC) and $\delta$(CNC)), symmetric $NH_2$ stretch ($\nu_s(NH_2)$), $NH_2$ bending ($\delta(NH_2)$), $NH_2$ wagging ($\omega(NH_2)$), $CH_3$ stretchings ($\nu_s(CH_3)$ and $\nu_{as}(CH_3)$) and $CH_3$ Bendings ($\delta_s(CH_3)$ and $\delta_{as}(CH_3)$). For $[SnBr_6]$, only $\nu_1$, $\nu_2$, $\nu_5$ and the librational mode (L) could be involved. Figure 10 shows the displacement vectors from the $B_{2g}$ irrep basis (scaled for better visibility) of both $[SnBr_6]^{2-}$ and $DMA^+$.

Figure 10 – Scaled displacement vectors from the $B_{2g}$ irrep basis for: a) the [$SnBr_6$] octahedra and b) the DMA molecule inside the unit cell.

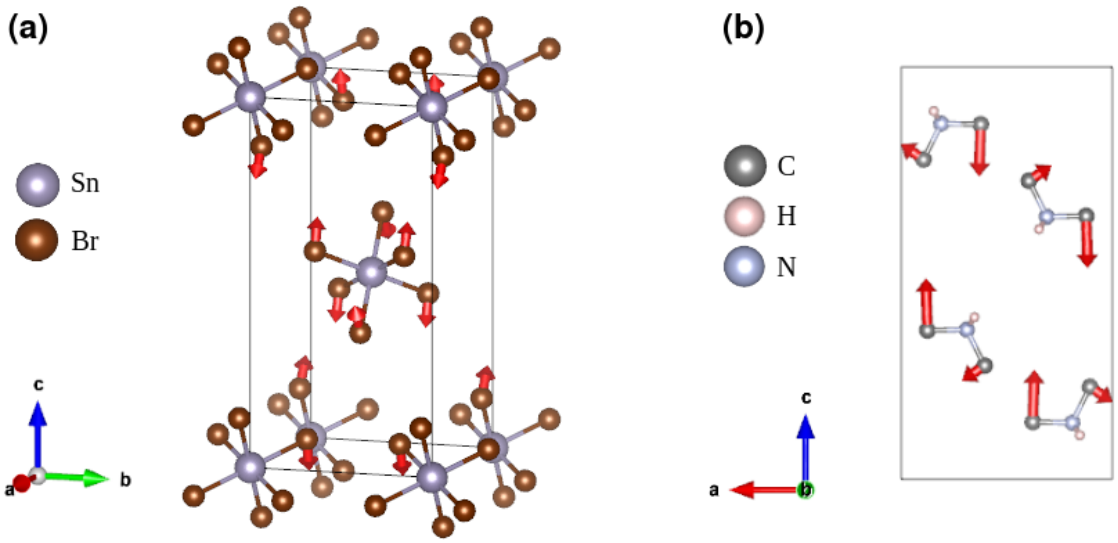


From the displacement vectors on Figure 10, the structural distortions of both components seem to be closely related to librational modes (L), however in the displacements of the DMA molecules (Figure 10b)), the $NH_2$ group stays fixed and the two carbon atoms have noticeably different displacement amplitudes, which shows that the final result contains the frozen displacement of a bending vibration of the C-N-C skeleton ($\delta$(CNC)).

Additionally, using the IR and Raman selection rules, we found that, for the high symmetry (orthorhombic) structure, the IR-active modes belong to the $B_{1u}$, $B_{2u}$ and $B_{3u}$ irreps, which (excluding the translational accoustic modes) make in total the 68 IR modes: $\Gamma^{IR} = 25B_{1u} + 18B_{2u} + 25B_u$, while the Raman-active modes belong to the $A_g$, $B_{1g}$, $B_{2g}$ and $B_{3g}$ irreps, totaling the 84 Raman modes: $\Gamma^{Raman} = 24A_g + 18B_{1g} + 24B_{2g} + 18B_{3g}$. Since the displacements that lead the phase transition have $B_{2g}$ symmetry, it is expected that the modes related to those will appear directly in the Raman spectrum.

### 4.3 Theoretical (DFPT) vibrational modes

To begin the theoretical investigation, the structure of $(DMA)_2SnBr_6$ was used in its orthorhombic 300 K phase, however, in order to use the structure in this high symmetry setting, the disordered hydrogens have been modified before the calculations. Instead of choosing one of the sets of three hydrogens, their final positions were chosen as the midpoint of each disordered pair of hydrogens.

The structure was then relaxed and the obtained structural parameters were: $a = 7.8089$ Å, $b = 7.6698$ Å and $c = 14.8194$ Å, which is in line with the usual overestimations from GGA DFT (FISCHER *et al.*, 2016). Finally the 174 modes were calculated in the framework of Density Functional Perturbation Theory (DFPT) at the Γ-point. The calculated theoretical frequencies and symmetries of each mode, together with their estimated IR intensities can be found in Appendix A.

From the initial results, it can already be seen that a total of seven theoretical frequencies were found to be imaginary, however three of those are the $B_{1u}$, $B_{2u}$ and $B_{3u}$ acoustic modes and furthermore their frequencies are close to zero, indicating that this can be taken as a small error in the calculation. Meanwhile, the other four modes can be seen on Figure 11 and they seem to actually indicate structure instability, which is further supported by the appearance of the mode $\nu_4$ ($B_{2g}$) that exactly matches the previously discussed $B_{2g}$ mode that drives the symmetry break in the orthorhombic (Pnmn) to monoclinic (P2/m) transition (see Figure 10).

Figure 11 – The first four calculated modes with imaginary frequency

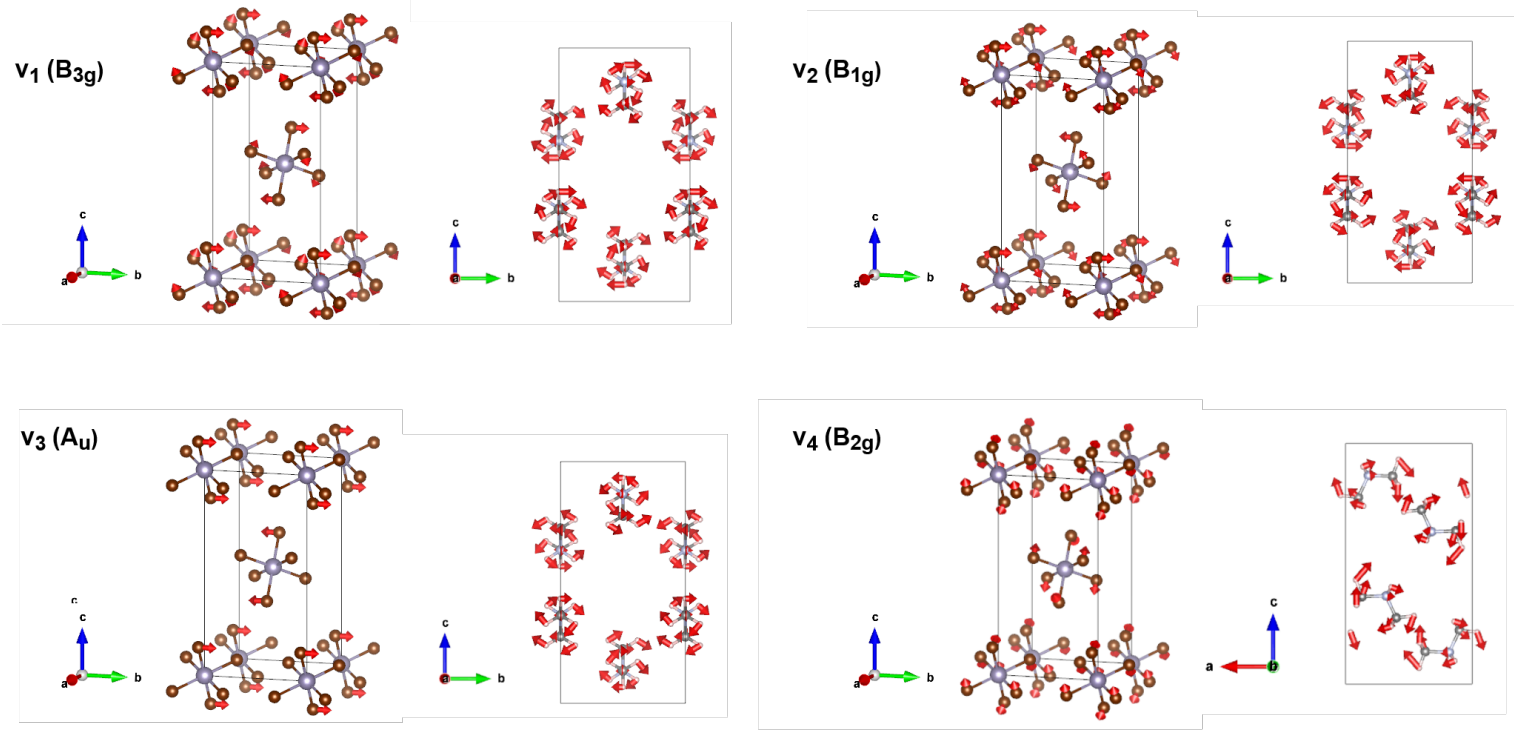


Following this interpretation, the other modes should also indicate the loss of other symmetries. In the case of the $\nu_1(B_{3g})$ and $\nu_2(B_{1g})$ modes, which in the monoclinic phase will both become $B_g$ modes (See Figure 12 a)), we clearly note that they are antisymmetric with respect to the $C_2$ axis and the $\sigma_h$ plane but symmetric with respect to the center of inversion $i$

(See Figure 12 b)), leading to the conclusion that these are the modes related to the monoclinic (P2/m) to triclinic ($P\bar{1}$) phase transition.

Figure 12 – a) Correlations between the orthorhombic phase ($D_{2h}$) and monoclinic phase ($C_{2h}$) irreducible representations and b) character table of the $C_{2h}$ point group

a)

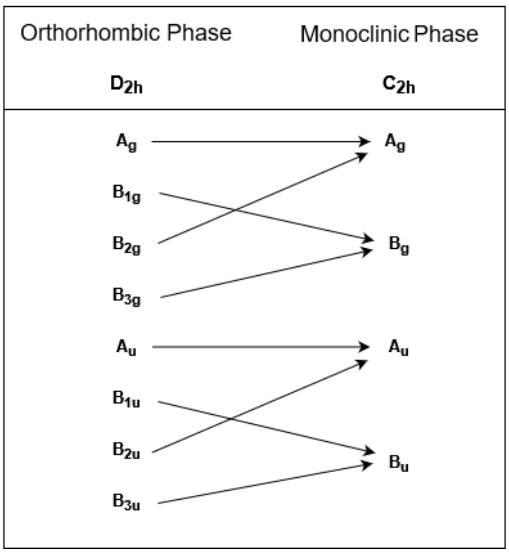


b)

| $C_{2h}(2/m)$ | E | $C_2$ | $\sigma_h$ | i |
|---|---|---|---|---|
| $A_g$ | 1 | 1 | 1 | 1 |
| $B_g$ | 1 | -1 | -1 | 1 |
| $A_u$ | 1 | 1 | -1 | -1 |
| $B_u$ | 1 | -1 | 1 | -1 |

These three modes alone are already in agreement with the experimentally observed phase transitions, however the extra $v_3(A_u)$ mode indicates yet another symmetry break, this time associated with the loss of the inversion center *i* (see Figure 12 b)) which would correspond to a new triclinic ($P\bar{1}$) to triclinic (P1) phase transition that was not observed in the temperature range investigated by our SCXRD measurements, but as will be discussed in the following section, appears to be linked to several events at $\sim$50 K in the Raman spectrum.

### 4.4 Temperature-dependent Raman Spectroscopy

We then start the investigation of the Raman spectra by analyzing the changes on the octahedral modes and the rigid body motions of the $DMA^+$ cations (translation and libration modes) displayed Figure 13. From our theoretical calculations (see Appendix A), the modes at 110 and 120 $cm^{-1}$ can be assigned as DMA translational modes (T), while the modes at 100, 140 and 186 $cm^{-1}$ can be respectively assigned as the octahedron's $\nu_5$ ($T_{2g}$), $\nu_2$ ($E_g$) and $\nu_1$ ($A_g$) modes. All modes show the standard softening on heating and, even though a discontinuous jump was observed both in the bond length distortion and in the angle distortion (see Figure 8 a)), the changes on the frequencies of the octahedral modes near the expected transition points (200 K and 100 K) were very small ($< 1$ $cm^{-1}$). This could be explained by the previously mentioned

fact that both Sn-Br bond lengths and Br-Sn-Br angles don't show sizable variations over the investigated temperature range.

Figure 13 – a): Temperature-dependent normalized Raman spectra obtained for $(DMA)_2SnBr_6$ between 10-290 K in the 100–195 $cm^{-1}$ range, b): Temperature-dependent behavior of the observed peak centers in this wavenumber region.

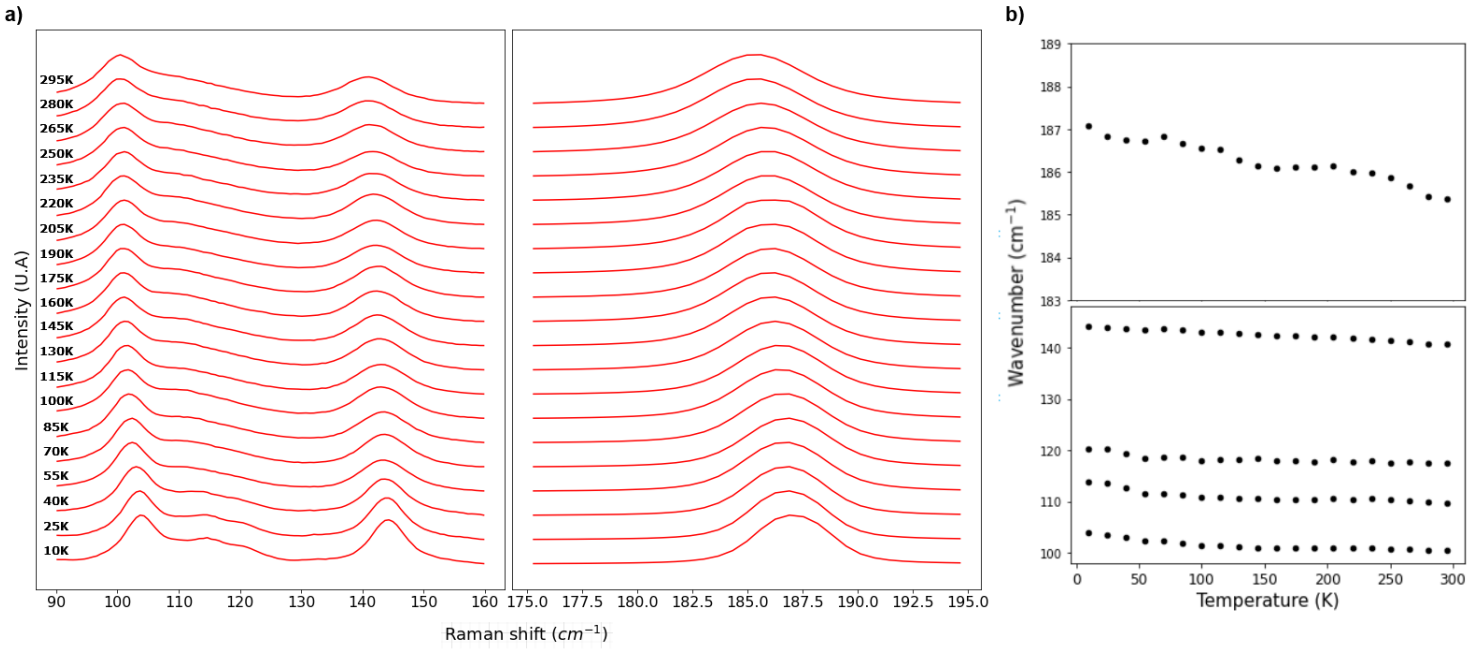


The 760–930 $cm^{-1}$ region shown on Figures 14 and 15 is assigned as a lower frequency region of the $DMA^+$ cation vibrations, where the first the modes appearing between 770 and 800 $cm^{-1}$ are associated with the $NH_2$ rocking mode($\rho(NH_2)$), the modes at 840, 860 and 885 $cm^{-1}$ are associated with the symmetric C-N-C stretchings ($\nu_s$(CNC)), the two modes at 895 $cm^{-1}$ are associated with the $NH_2$ torsions ($\tau(NH_2)$) and the mode at 915 $cm^{-1}$ could be associated with the assymetrical C-N-C stretchings ($\nu_{as}$(CNC). In this region, most of the observed modes suffer a bigger discontinuous softening of about 1-2 $cm^{-1}$ near 200 K, except for the $\tau(NH_2)$ modes that appear to be the least sensible to the distortions of the orthorhombic-monoclinic transition, however, the event that appears at 280 K (Figure 15) matches the previously observed discontinuous jump in the lattice parameter c (Figure 6 b)) and in the octahedral distortions (Figure 8 a)), therefore, this can be attributed to the coupling between octahedrons to the DMA Molecules through the N-H ... $[SnBr_6]$ hydrogen bonds (see Figure 9) that form in this structure.

Figure 15 also shows weaker discontinuities at $\sim$ 160 K, which wasn't observed in any of the previous measurements but it cannot be a phase transition since the structure was

Figure 14 – a): Temperature-dependent normalized Raman spectra obtained for $(DMA)_2SnBr_6$ between 10-290 K in the 760–880 $cm^{-1}$ range, b): Temperature-dependent behavior of the observed peak centers in this wavenumber region.

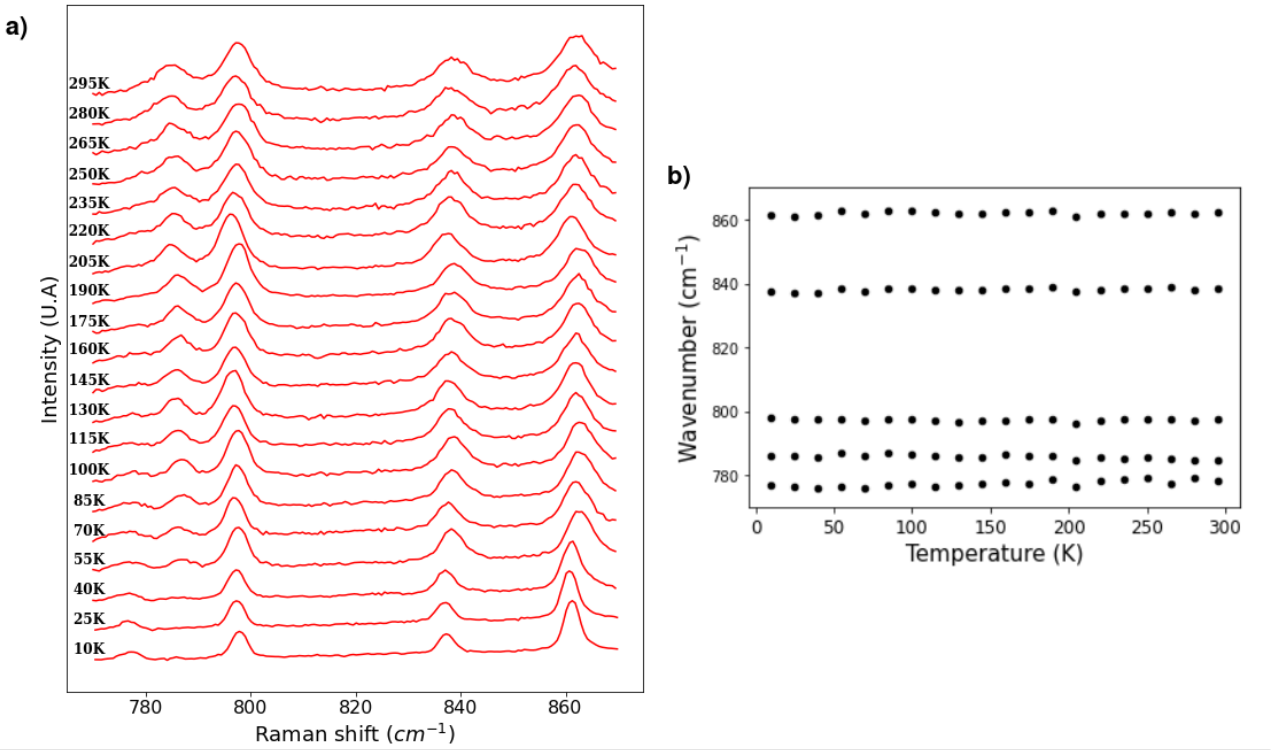


Figure 15 – a): Temperature-dependent normalized Raman spectra obtained for $(DMA)_2SnBr_6$ between 10-290 K in the 870–930 $cm^{-1}$ range, b): Temperature-dependent behavior of the observed peak centers in this wavenumber region.

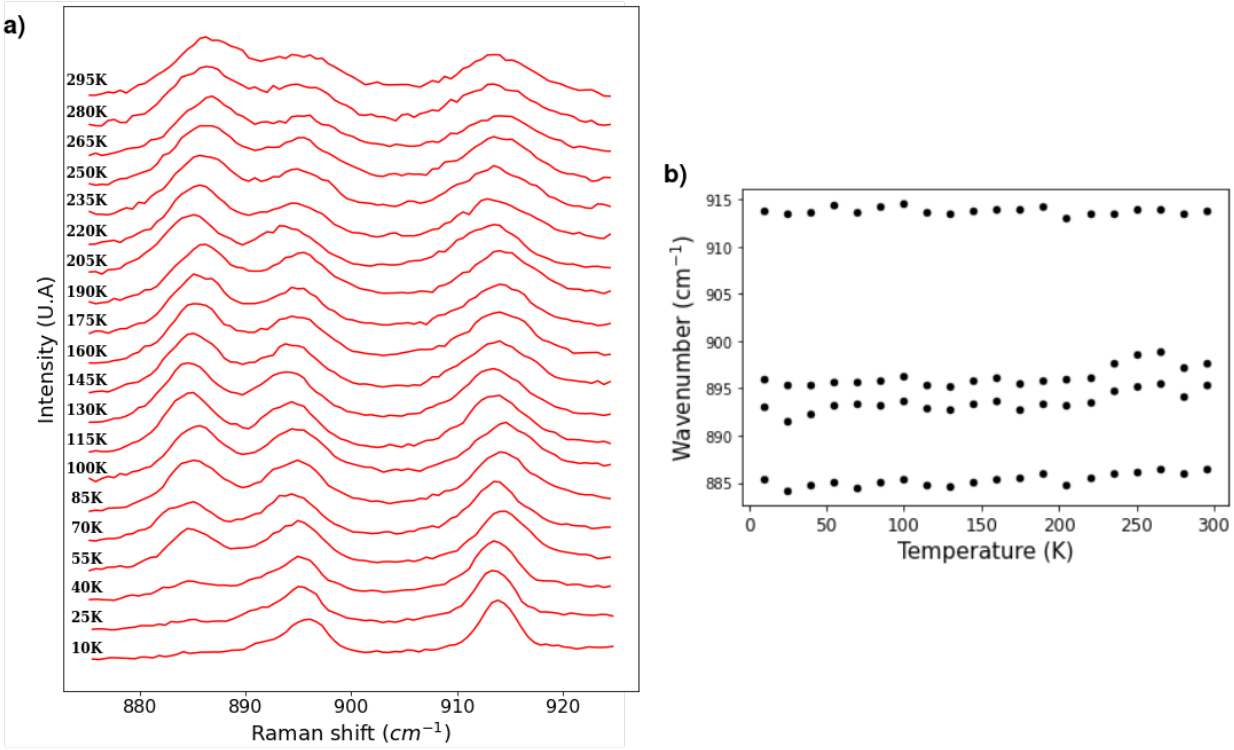

still found to be monoclinic between 160 K and 130 K, and at $\sim$ 100 K which could be the monoclinic-triclinic phase transition, but the most important feature of this region seems to be changes at $\sim$50 K, where some discontinuities appear on the frequencies and most remarkably, the relative intensities of the peaks change abruptly, especially to the peaks at 790 and 885 $cm^{-1}$ which almost vanish below 55 K. This event seems to repeat in other regions as well, allowing us to attribute it as the triclinic ($P\bar{1}$) to triclinic (P1) phase transition that was found in our theoretical calculations.

In Figure 16 the first three modes can be assigned as the asymmetric C-N-C stretchings ($\nu_{as}$(CNC)) while above 1000 $cm^{-1}$ we have the beginning of the $CH_3$ rocking modes which continues in Figures 17 and 18. Again, many peaks show a discontinuous softening close to 200 K, but differently from other regions, we identify a splitting of the peak at 1060 $cm^{-1}$, most likely occurring due to the appearance of a second symmetry independent DMA molecule in the unit cell (see Figure 8 b)). Together with the $NH_2$ modes, the $CH_3$ modes are also regarded as especially susceptible to changes in the hydrogen bonds between the DMA cation and the inorganic framework (RODRÍGUEZ-HERNÁNDEZ *et al.*, 2022), therefore the discontinuities observed in this region provide a complement to the previous analysis by showing the involvement of the disordered hydrogens from the $CH_3$ group in all the previously observed events, with Figures 17 and 18 even showing the events close to 280 K which were previously attributed to the change in octahedral distortions affecting the hydrogen bonds with the $NH_2$ group. However, even though a few peaks show softenings that could indicate the order-disorder (monoclinic-triclinic) phase transition are observed around 100 K (see Figure 17), they are still weaker when compared to the softening at 200 K caused by the displacive (orthorhombic-monoclinic) phase transition, revealing that the ordering of the hydrogens doesn't cause very significant changes in the C-H interactions.

Figure 16 – a): Temperature-dependent normalized Raman spectra obtained for $(DMA)_2SnBr_6$ between 10-290 K in the 980–1080 $cm^{-1}$ range, b): Temperature-dependent behavior of the observed peak centers in this wavenumber region.

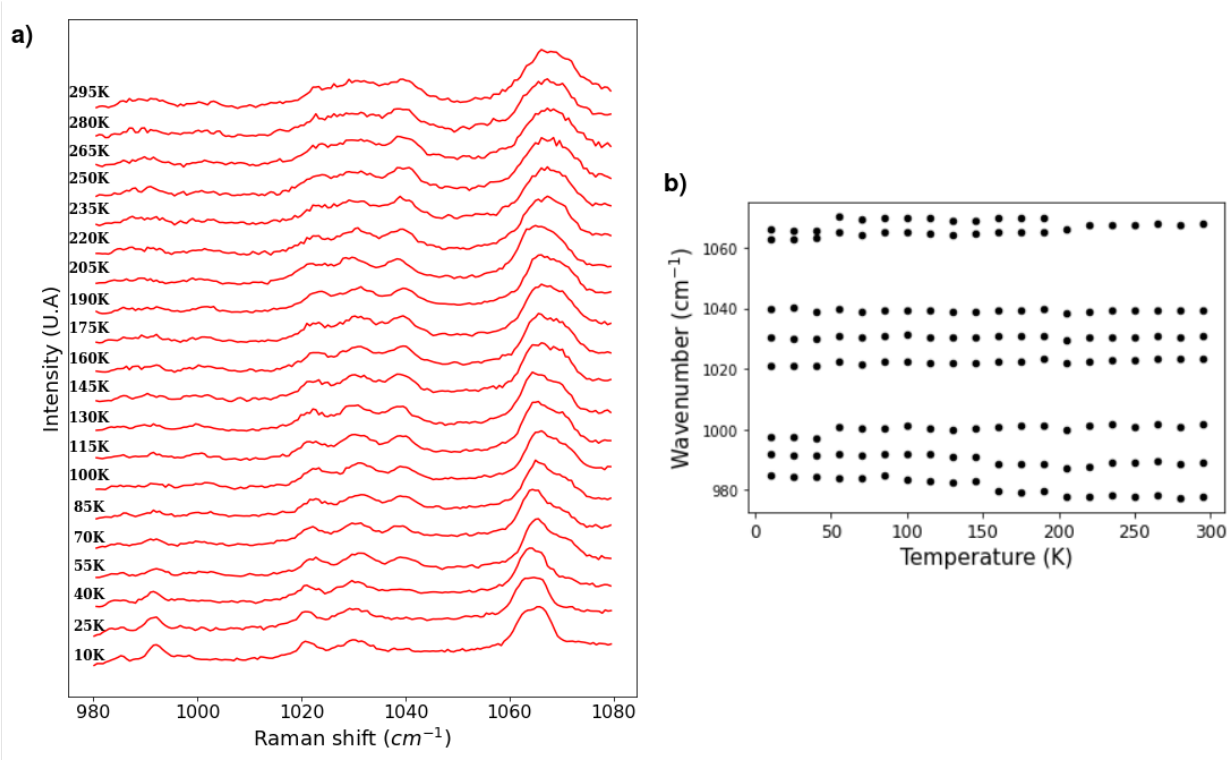


Figure 17 – a): Temperature-dependent normalized Raman spectra obtained for $(DMA)_2SnBr_6$ between 10-290 K in the 1140–1190 $cm^{-1}$ range, b): Temperature-dependent behavior of the observed peak centers in this wavenumber region.

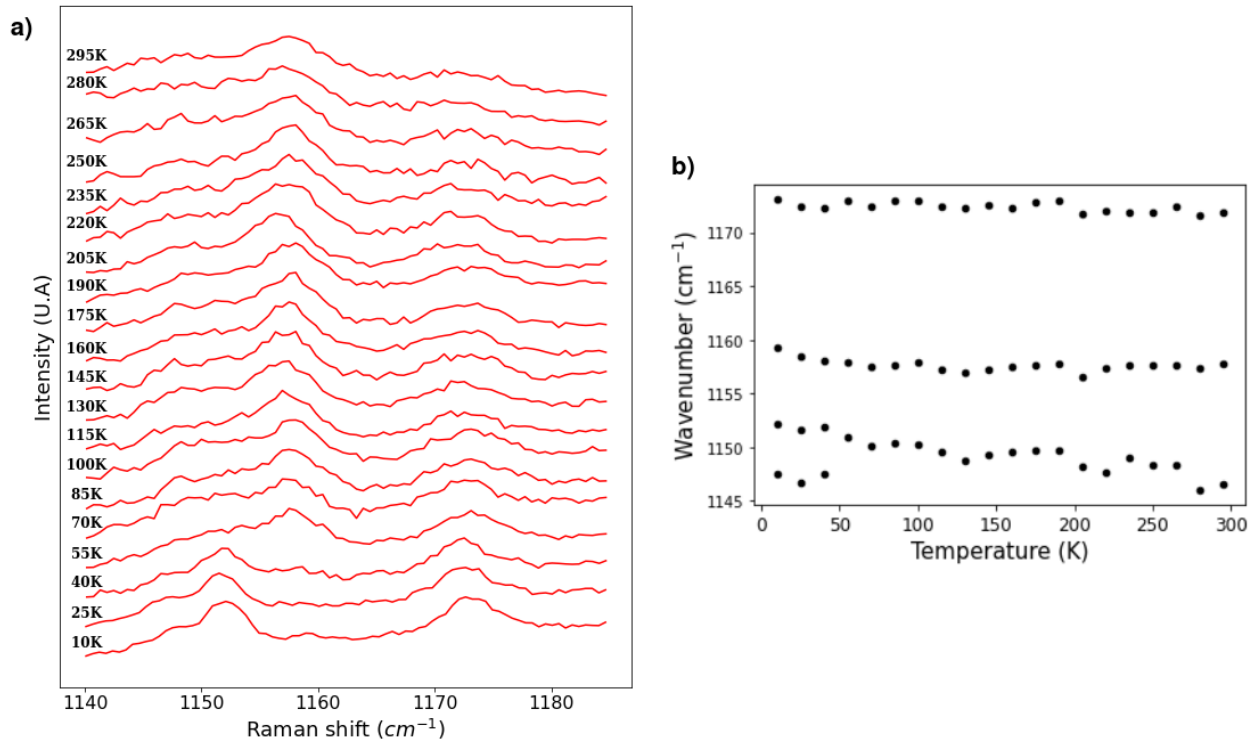

Figure 18 – a): Temperature-dependent normalized Raman spectra obtained for $(DMA)_2SnBr_6$ between 10-290 K in the 1280–1360 $cm^{-1}$ range, b): Temperature-dependent behavior of the observed peak centers in this wavenumber region.

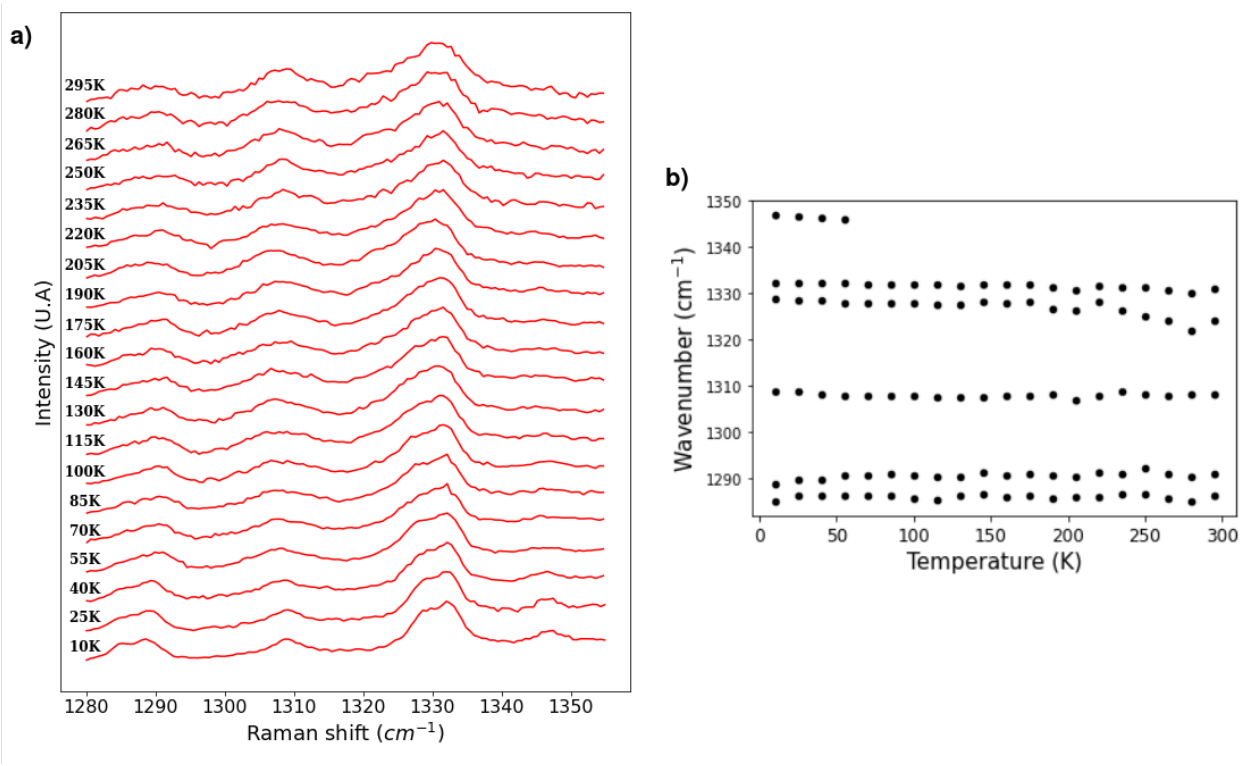


Figure 19 shows the region of the symmetrical and asymmetrical $CH_3$ bending modes ($\delta_s(CH_3)$ and $\delta_{as}(CH_3)$). Again, the phase transition at 200 K (orthorhombic-monoclinic) appears as a discontinuous jump in the frequencies of all the observed modes, however, all modes in this region also suffer an unusual hardening on heating which could be explained by the weakening of the hydrogen bonds on higher temperatures, reducing the coupling between the organic and inorganic components and leading to the observed frequency increases. This region also shows a notable splitting of the mode at 1440 $cm^{-1}$ event occurring at 100 K, which could be linked with the order-disorder phase transition.

The last three regions displayed in Figures 20, 21 and 22 are associated with the higher frequency modes of the DMA molecule, i.e. the $CH_3$ and $NH_2$ stretchings ($\nu_s$ ($CH_3$), $\nu_{as}$ ($CH_3$), $\nu_s$ ($NH_2$) and $\nu_{as}$ ($NH_2$)). In these regions, the events at 50 K become more visible with substantial frequency shifts appearing on Figure 20. The modes in the 3080 - 3220 $cm^{-1}$ (Figure 22) range seem to be the least affected by the 200 K transition (orthorhombic-monoclinic), however this is expected, since these modes are associated with the $NH_2$ stretchings and the $NH_2$ group was the least involved in the displacements that lead the transition (see Figure 10 b)).

Figure 19 – a): Temperature-dependent normalized Raman spectra obtained for $(DMA)_2SnBr_6$ between 10-290 K in the 1420–1480 $cm^{-1}$ range, b): Temperature-dependent behavior of the observed peak centers in this wavenumber region.

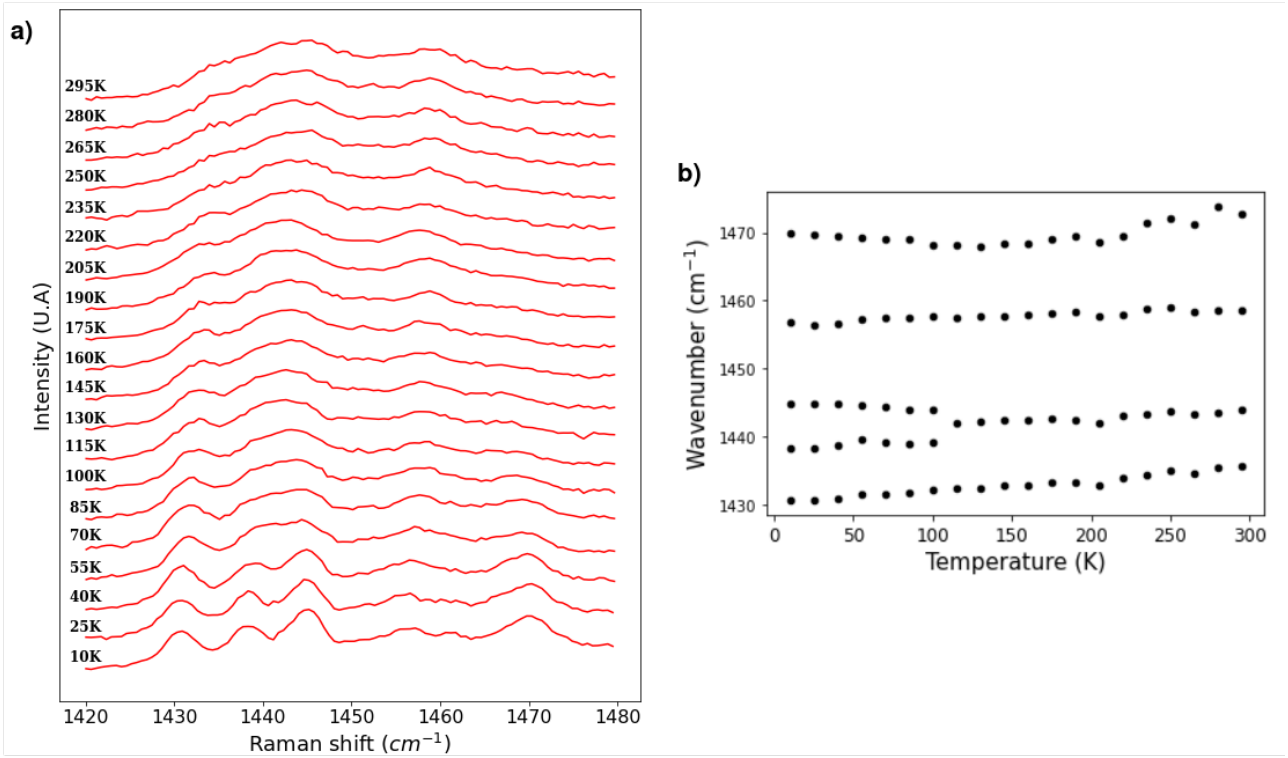


Figure 20 – a): Temperature-dependent normalized Raman spectra obtained for $(DMA)_2SnBr_6$ between 10-290 K in the 2840–2950 $cm^{-1}$ range, b): Temperature-dependent behavior of the observed peak centers in this wavenumber region.

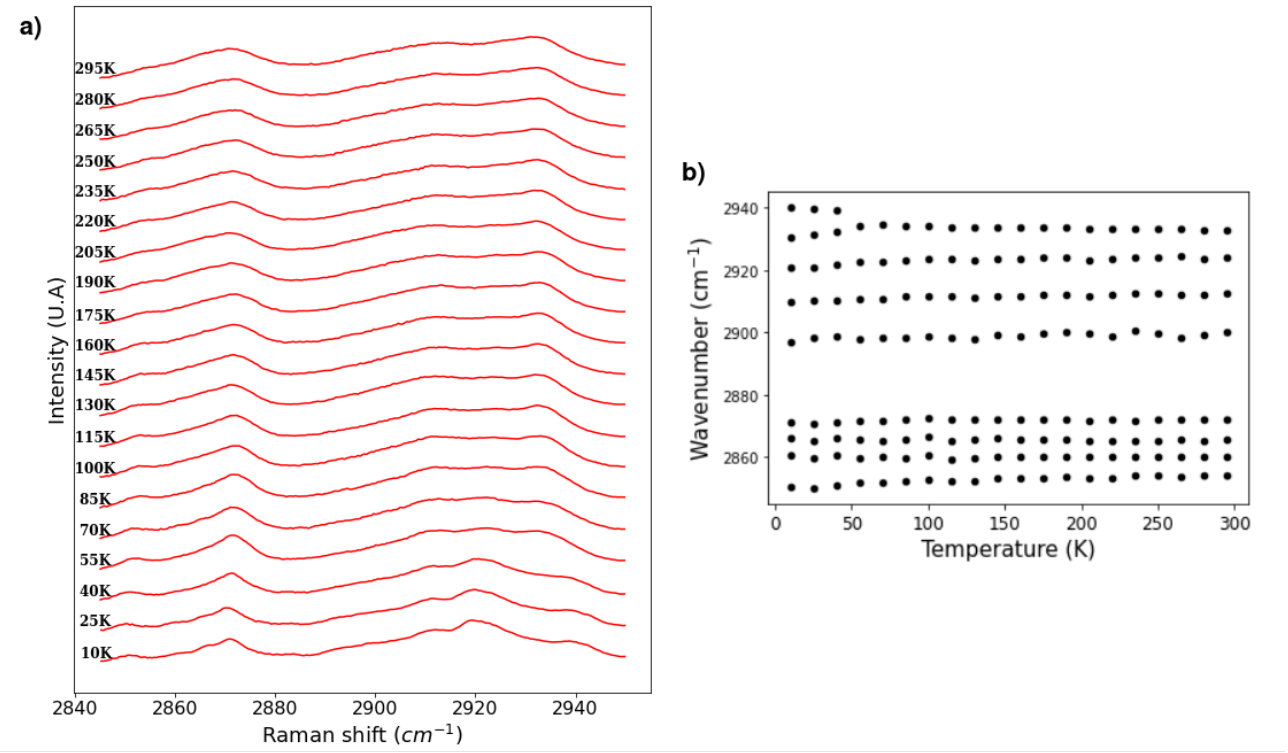

Figure 21 – a): Temperature-dependent normalized Raman spectra obtained for $(DMA)_2SnBr_6$ between 10-290 K in the 2950–3020 $cm^{-1}$ range, b): Temperature-dependent behavior of the observed peak centers in this wavenumber region.

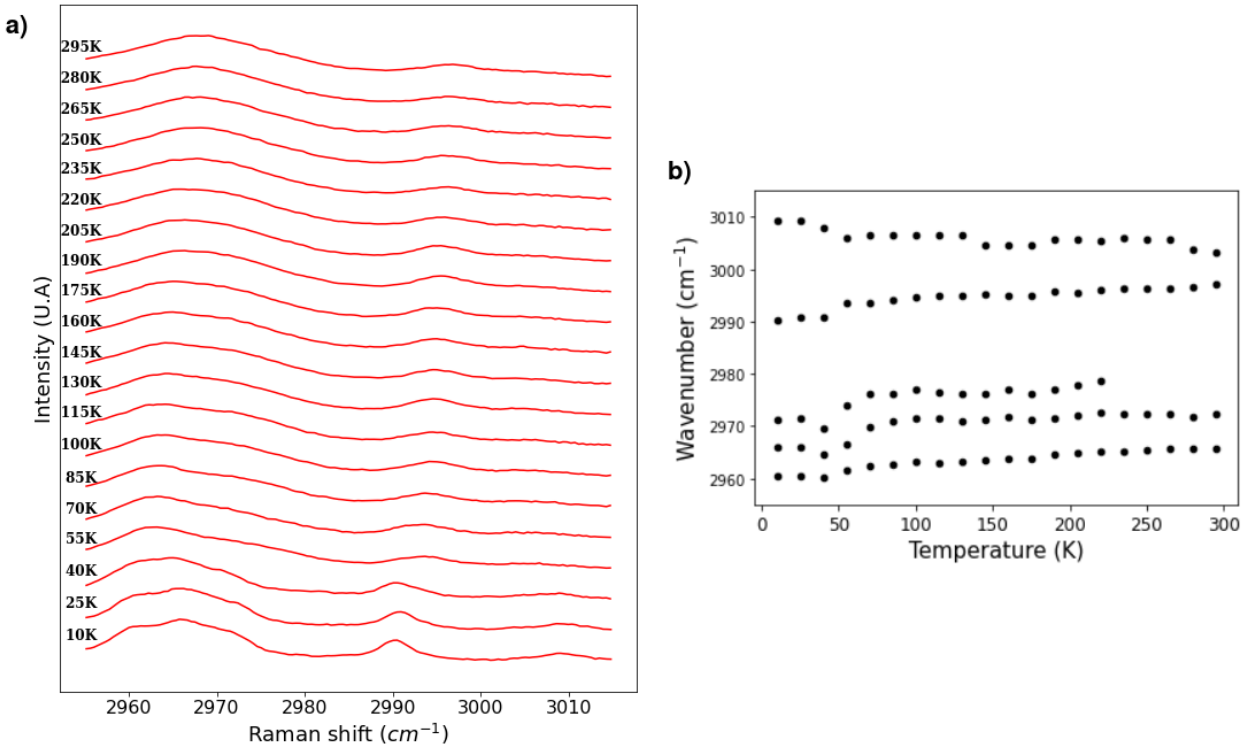


Figure 22 – a): Temperature-dependent normalized Raman spectra obtained for $(DMA)_2SnBr_6$ between 10-290 K in the 3080–3220 $cm^{-1}$ range, b): Temperature-dependent behavior of the observed peak centers in this wavenumber region.

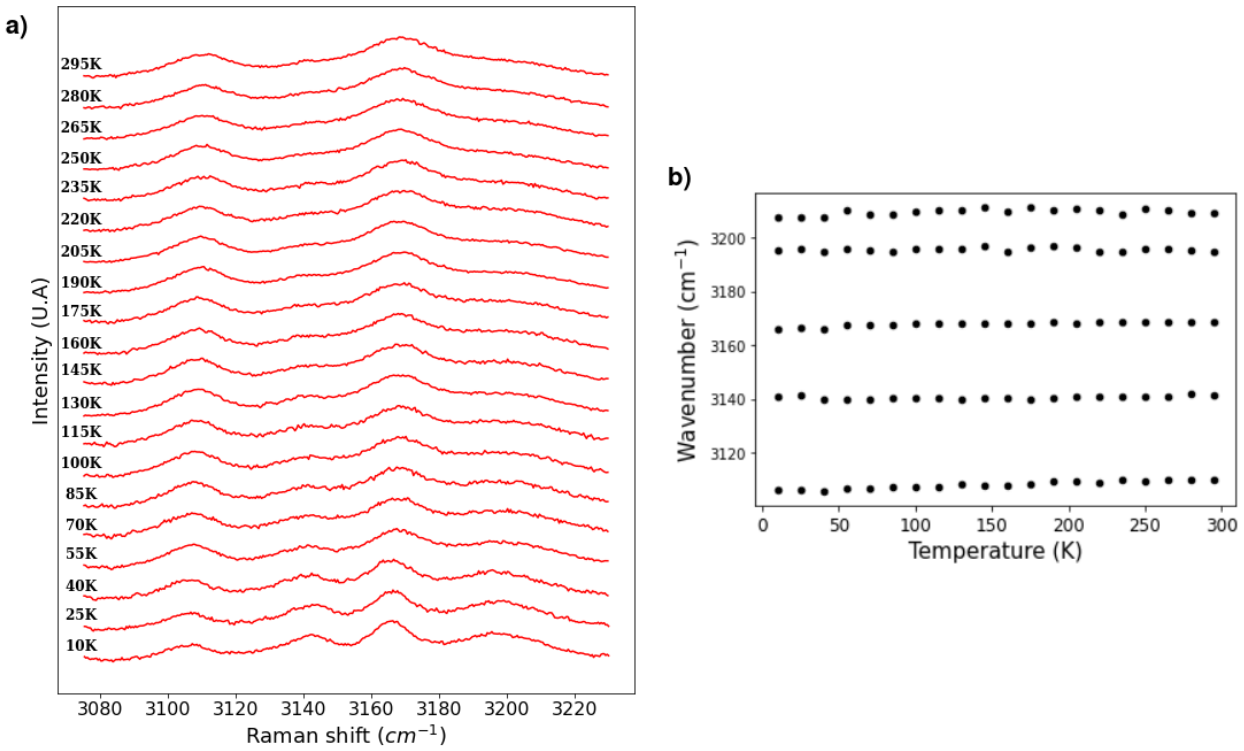

# 5 CONCLUSIONS

The analysis of the phase transitions of $(DMA)_2SnBr_6$ existing between 10 K and 300 K was carried out. Temperature-dependent SCXRD and DSC measurements revealed an orthorhombic (Pnmn) to monoclinic (P2/m) displacive phase transition and a monoclinic (P2/m) to triclinic ($P\bar{1}$) order-disorder phase transition which, based on the events observed on the Raman spectrum, were found to happen at $\sim$200 K and $\sim$100 K, respectively. The displacive phase transition was further studied through a symmetry mode analysis which reveald the primary mode i.e. the collective displacements that lead to the symmetry break in the orthorhombic to monoclinic phase transition, which was later found as an unstable mode in our theoretical $\Gamma$-point phonon calculations. Additionaly, the phonon calculations also predict another triclinic ($P\bar{1}$) -> triclinic (P1) that was confirmed to be at $\sim$50 K by the Raman measurements.

## REFERENCES

ALTINKAYA, C.; AYDIN, E.; UGUR, E.; ISIKGOR, F. H.; SUBBIAH, A. S.; BASTIANI, M. D.; LIU, J.; BABAYIGIT, A.; ALLEN, T. G.; LAQUAI, F. *et al.* Tin oxide electron-selective layers for efficient, stable, and scalable perovskite solar cells. **Advanced Materials**, Wiley Online Library, v. 33, n. 15, p. 2005504, 2021.

ARFKEN, G. B.; WEBER, H. J.; HARRIS, F. E. **Mathematical Methods for Physicists**: a comprehensive guide. 7. ed. [S.l.]: Academic Press, 2012.

BHUMLA, P.; JAIN, M.; SHEORAN, S.; BHATTACHARYA, S. Vacancy-ordered double perovskites cs2bi6 (b= pt, pd, te, sn): An emerging class of thermoelectric materials. **The Journal of Physical Chemistry Letters**, ACS Publications, v. 13, n. 50, p. 11655–11662, 2022.

BURGER, S.; EHRENREICH, M.; KIESLICH, G. Tolerance factors of hybrid organic–inorganic perovskites: recent improvements and current state of research. **Journal of Materials Chemistry A**, Royal Society of Chemistry, v. 6, n. 44, p. 21785–21793, 2018.

CEPERLEY, D. M.; ALDER, B. J. Ground state of the electron gas by a stochastic method. **Physical review letters**, APS, v. 45, n. 7, p. 566, 1980.

CHOWDHURY, T. H.; REO, Y.; YUSOFF, A. R. B. M.; NOH, Y.-Y. Sn-based perovskite halides for electronic devices. **Advanced Science**, Wiley Online Library, v. 9, n. 33, p. 2203749, 2022.

COHEN-TANNOUDJI, C.; DIU, B.; LALOË, F. **Quantum Mechanics**. 2. ed. [S.l.]: Wiley-VCH, 2019.

DOLOMANOV, O. V.; BOURHIS, L. J.; GILDEA, R. J.; HOWARD, J. A.; PUSCHMANN, H. Olex2: a complete structure solution, refinement and analysis program. **Journal of applied crystallography**, International Union of Crystallography, v. 42, n. 2, p. 339–341, 2009.

DONG, Q.; FANG, Y.; SHAO, Y.; MULLIGAN, P.; QIU, J.; CAO, L.; HUANG, J. Electron-hole diffusion lengths> 175 $\mu$m in solution-grown ch3nh3pbi3 single crystals. **Science**, American Association for the Advancement of Science, v. 347, n. 6225, p. 967–970, 2015.

EL-MELLOUHI, F.; MARZOUK, A.; BENTRIA, E. T.; RASHKEEV, S. N.; KAIS, S.; ALHARBI, F. H. Hydrogen bonding and stability of hybrid organic–inorganic perovskites. **ChemSusChem**, Wiley Online Library, v. 9, n. 18, p. 2648–2655, 2016.

FAIZAN, M.; BHAMU, K.; MURTAZA, G.; HE, X.; KULHARI, N.; AL-ANAZY, M. M.; KHAN, S. H. Electronic and optical properties of vacancy ordered double perovskites a2bx6 (a= rb, cs; b= sn, pd, pt; and x= cl, br, i): a first principles study. **Scientific reports**, Nature Publishing Group UK London, v. 11, n. 1, p. 6965, 2021.

FAIZAN, M.; BHAMU, K.; MURTAZA, G.; HE, X.; KULHARI, N.; AL-ANAZY, M. M.; KHAN, S. H. Electronic and optical properties of vacancy ordered double perovskites a2bx6 (a= rb, cs; b= sn, pd, pt; and x= cl, br, i): a first principles study. **Scientific reports**, Nature Publishing Group UK London, v. 11, n. 1, p. 6965, 2021.

FAIZAN, M.; WANG, X.; ABDELMOHSEN, S. A.; BHAMU, K.; SAPPATI, S.; LAREF, A.; MUHAMMAD, N.; MUSHTAQ, M.; ABDELBACKI, A. M.; KHENATA, R. Understanding the electronic structure and optical properties of vacancy-ordered double perovskite a2bx6 for

optoelectronic applications. **Energy & Fuels**, ACS Publications, v. 36, n. 13, p. 7065–7074, 2022.

FISCHER, M.; EVERS, F. O.; FORMALIK, F.; OLEJNICZAK, A. Benchmarking dft-gga calculations for the structure optimisation of neutral-framework zeotypes. **Theoretical Chemistry Accounts**, Springer, v. 135, p. 1–19, 2016.

GIANNOZZI, P.; ANDREUSSI, O.; BRUMME, T.; BUNAU, O.; NARDELLI, M. B.; CALANDRA, M.; CAR, R.; CAVAZZONI, C.; CERESOLI, D.; COCOCCIONI, M. *et al.* Advanced capabilities for materials modelling with quantum espresso. **Journal of physics:** condensed matter, IOP Publishing, v. 29, n. 46, p. 465901, 2017.

GIANNOZZI, P.; BARONI, S. Density-functional perturbation theory. *In*: **Handbook of Materials Modeling**: methods. [S.l.]: Springer, 2005. p. 195–214.

GIANNOZZI, P.; BARONI, S.; BONINI, N.; CALANDRA, M.; CAR, R.; CAVAZZONI, C.; CERESOLI, D.; CHIAROTTI, G. L.; COCOCCIONI, M.; DABO, I. *et al.* Quantum espresso: a modular and open-source software project for quantum simulations of materials. **Journal of physics: Condensed matter**, IOP Publishing, v. 21, n. 39, p. 395502, 2009.

GLOCKZIN, B.; OAKLEY, M. S.; KARMAKAR, A.; POMINOV, A.; MITCHELL, A. A.; MA, X.; KLOBUKOWSKI, M.; MICHAELIS, V. K. Alkali tin halides: Exploring the local structure of a2snx6 (a= k, rb; x= cl, br, i) compounds using solid-state nmr and dft computations. **The Journal of Physical Chemistry C**, ACS Publications, v. 127, n. 15, p. 7284–7298, 2023.

GOLDSCHMIDT, V. M. Die gesetze der krystallochemie. **Naturwissenschaften**, Springer, v. 14, n. 21, p. 477–485, 1926.

GREEN, M. A.; HO-BAILLIE, A.; SNAITH, H. J. The emergence of perovskite solar cells. **Nature photonics**, Nature Publishing Group UK London, v. 8, n. 7, p. 506–514, 2014.

HAMANN, D. Optimized norm-conserving vanderbilt pseudopotentials. **Physical Review B**, APS, v. 88, n. 8, p. 085117, 2013.

HEID, R. 12 density functional perturbation theory and electron phonon coupling. In: . [s.n.], 2013. Available at: https://api.semanticscholar.org/CorpusID:13680216.

HOHENBERG, P.; KOHN, W. Inhomogeneous electron gas. **Physical review**, APS, v. 136, n. 3B, p. B864, 1964.

KALTZOGLOU, A.; ANTONIADOU, M.; KONTOS, A. G.; STOUMPOS, C. C.; PERGANTI, D.; SIRANIDI, E.; RAPTIS, V.; TROHIDOU, K.; PSYCHARIS, V.; KANATZIDIS, M. G. *et al.* Optical-vibrational properties of the cs2snx6 (x= cl, br, i) defect perovskites and hole-transport efficiency in dye-sensitized solar cells. **The Journal of Physical Chemistry C**, ACS Publications, v. 120, n. 22, p. 11777–11785, 2016.

KATZ, E. A. Perovskite: name puzzle and german-russian odyssey of discovery. **Helvetica Chimica Acta**, Wiley Online Library, v. 103, n. 6, p. e2000061, 2020.

KHALFIN, S.; BEKENSTEIN, Y. Advances in lead-free double perovskite nanocrystals, engineering band-gaps and enhancing stability through composition tunability. **Nanoscale**, v. 11, n. 18, p. 8665–8679, 2019.

KIESLICH, G.; SUN, S.; CHEETHAM, A. K. Solid-state principles applied to organic–inorganic perovskites: new tricks for an old dog. **Chemical Science**, Royal Society of Chemistry, v. 5, n. 12, p. 4712–4715, 2014.

KLEIN, O. Elektrodynamik und wellenmechanik vom standpunkt des korrespondenzprinzips. **Zeitschrift für Physik A Hadrons and nuclei**, Springer, v. 41, n. 6-7, p. 407–442, 1927.

KOHN, W.; SHAM, L. J. Self-consistent equations including exchange and correlation effects. **Physical review**, APS, v. 140, n. 4A, p. A1133, 1965.

KONINGSTEIN, J. A. **Introduction to the Theory of the Raman Effect**. [S.l.]: Springer Science & Business Media, 2012.

KRAUSE, L.; HERBST-IRMER, R.; SHELDRICK, G. M.; STALKE, D. Comparison of silver and molybdenum microfocus x-ray sources for single-crystal structure determination. **Journal of applied crystallography**, International Union of Crystallography, v. 48, n. 1, p. 3–10, 2015.

LEE, B.; STOUMPOS, C. C.; ZHOU, N.; HAO, F.; MALLIAKAS, C.; YEH, C.-Y.; MARKS, T. J.; KANATZIDIS, M. G.; CHANG, R. P. Air-stable molecular semiconducting iodosalts for solar cell applications: Cs2sni6 as a hole conductor. **Journal of the American Chemical Society**, ACS Publications, v. 136, n. 43, p. 15379–15385, 2014.

LIAO, Y.; LIU, H.; ZHOU, W.; YANG, D.; SHANG, Y.; SHI, Z.; LI, B.; JIANG, X.; ZHANG, L.; QUAN, L. N. *et al.* Highly oriented low-dimensional tin halide perovskites with enhanced stability and photovoltaic performance. **Journal of the American Chemical Society**, ACS Publications, v. 139, n. 19, p. 6693–6699, 2017.

LIU, T.; ZONG, Y.; ZHOU, Y.; YANG, M.; LI, Z.; GAME, O. S.; ZHU, K.; ZHU, R.; GONG, Q.; PADTURE, N. P. High-performance formamidinium-based perovskite solar cells via microstructure-mediated $\delta$-to-$\alpha$ phase transformation. **Chemistry of Materials**, ACS Publications, v. 29, n. 7, p. 3246–3250, 2017.

MACRAE, C. F.; SOVAGO, I.; COTTRELL, S. J.; GALEK, P. T.; MCCABE, P.; PIDCOCK, E.; PLATINGS, M.; SHIELDS, G. P.; STEVENS, J. S.; TOWLER, M. *et al.* Mercury 4.0: From visualization to analysis, design and prediction. **Journal of applied crystallography**, International Union of Crystallography, v. 53, n. 1, p. 226–235, 2020.

MAUGHAN, A. E.; GANOSE, A. M.; SCANLON, D. O.; NEILSON, J. R. Perspectives and design principles of vacancy-ordered double perovskite halide semiconductors. **Chemistry of Materials**, ACS Publications, v. 31, n. 4, p. 1184–1195, 2019.

MAUGHAN, A. E.; GANOSE, A. M.; SCANLON, D. O.; NEILSON, J. R. Perspectives and design principles of vacancy-ordered double perovskite halide semiconductors. **Chemistry of Materials**, ACS Publications, v. 31, n. 4, p. 1184–1195, 2019.

MOMMA, K.; IZUMI, F. Vesta 3 for three-dimensional visualization of crystal, volumetric and morphology data. **Journal of applied crystallography**, International Union of Crystallography, v. 44, n. 6, p. 1272–1276, 2011.

NISHIMURA, K.; KAMARUDIN, M. A.; HIROTANI, D.; HAMADA, K.; SHEN, Q.; IIKUBO, S.; MINEMOTO, T.; YOSHINO, K.; HAYASE, S. Lead-free tin-halide perovskite solar cells with 13% efficiency. **Nano Energy**, Elsevier, v. 74, p. 104858, 2020.

NOEL, N. K.; STRANKS, S. D.; ABATE, A.; WEHRENFENNIG, C.; GUARNERA, S.; HAGHIGHIRAD, A.-A.; SADHANALA, A.; EPERON, G. E.; PATHAK, S. K.; JOHNSTON, M. B. *et al.* Lead-free organic–inorganic tin halide perovskites for photovoltaic applications. **Energy & Environmental Science**, Royal Society of Chemistry, v. 7, n. 9, p. 3061–3068, 2014.

NOH, J. H.; IM, S. H.; HEO, J. H.; MANDAL, T. N.; SEOK, S. I. Chemical management for colorful, efficient, and stable inorganic–organic hybrid nanostructured solar cells. **Nano letters**, ACS Publications, v. 13, n. 4, p. 1764–1769, 2013.

OROBENGOA, D.; CAPILLAS, C.; AROYO, M. I.; PEREZ-MATO, J. M. Amplimodes: symmetry-mode analysis on the bilbao crystallographic server. **Journal of Applied Crystallography**, International Union of Crystallography, v. 42, n. 5, p. 820–833, 2009.

PERDEW, J. P.; BURKE, K.; WANG, Y. Generalized gradient approximation for the exchange-correlation hole of a many-electron system. **Physical review B**, APS, v. 54, n. 23, p. 16533, 1996.

PERDEW, J. P.; ERNZERH, M.; BURKE, K. Rationale for mixing exact exchange with density functional approximations. **The Journal of Chemical Physics**, p. 4, 1996.

PEREZ-MATO, J.; OROBENGOA, D.; AROYO, M. Mode crystallography of distorted structures. **Acta Crystallographica Section A:** foundations and advances, International Union of Crystallography, v. 66, n. 5, p. 558–590, 2010.

PLACZEK, G. **The rayleigh and raman scattering**. [S.l.]: Lawrence Radiation Laboratory, 1959.

RICCIARELLI, D.; MEGGIOLARO, D.; AMBROSIO, F.; ANGELIS, F. D. Instability of tin iodide perovskites: bulk p-doping versus surface tin oxidation. **ACS Energy Letters**, ACS Publications, v. 5, n. 9, p. 2787–2795, 2020.

RODRÍGUEZ-HERNÁNDEZ, J. S.; GÓMEZ, M. A.; ABREU, D.; NONATO, A.; SILVA, R. X. da; GARCIA-FERNANDEZ, A.; SENARIS-RODRIGUEZ, M. A.; SANCHEZ-ANDUJAR, M.; AYALA, A.; PASCHOAL, C. Uniaxial negative thermal expansion in the [(ch 3) 2 nh 2] pbbr 3 hybrid perovskite. **Journal of Materials Chemistry C**, Royal Society of Chemistry, v. 10, n. 46, p. 17567–17576, 2022.

SHELDRICK, G. M. A short history of shelx. **Acta Crystallographica Section A:** foundations of crystallography, International Union of Crystallography, v. 64, n. 1, p. 112–122, 2008.

SHELDRICK, G. M. Shelxt–integrated space-group and crystal-structure determination. **Acta Crystallographica Section A:** foundations and advances, International Union of Crystallography, v. 71, n. 1, p. 3–8, 2015.

SNAITH, H. J. Perovskites: the emergence of a new era for low-cost, high-efficiency solar cells. **The journal of physical chemistry letters**, ACS Publications, v. 4, n. 21, p. 3623–3630, 2013.

SONG, T.-B.; YOKOYAMA, T.; STOUMPOS, C. C.; LOGSDON, J.; CAO, D. H.; WASIELEWSKI, M. R.; ARAMAKI, S.; KANATZIDIS, M. G. Importance of reducing vapor atmosphere in the fabrication of tin-based perovskite solar cells. **Journal of the American Chemical Society**, ACS Publications, v. 139, n. 2, p. 836–842, 2017.

TAN, Z.; LI, J.; ZHANG, C.; LI, Z.; HU, Q.; XIAO, Z.; KAMIYA, T.; HOSONO, H.; NIU, G.; LIFSHITZ, E. *et al.* Highly efficient blue-emitting bi-doped cs2sncl6 perovskite variant: photoluminescence induced by impurity doping. **Advanced Functional Materials**, Wiley Online Library, v. 28, n. 29, p. 1801131, 2018.

WANG, T.; YAN, F. Reducing agents for improving the stability of sn-based perovskite solar cells. **Chemistry–An Asian Journal**, Wiley Online Library, v. 15, n. 10, p. 1524–1535, 2020.

WOJDYR, M. Fityk: a general-purpose peak fitting program. **Journal of applied crystallography**, International Union of Crystallography, v. 43, n. 5, p. 1126–1128, 2010.

ZHAO, X.-G.; YANG, J.-H.; FU, Y.; YANG, D.; XU, Q.; YU, L.; WEI, S.-H.; ZHANG, L. Design of lead-free inorganic halide perovskites for solar cells via cation-transmutation. **Journal of the American Chemical Society**, ACS Publications, v. 139, n. 7, p. 2630–2638, 2017.

ZHU, H.; MA, J.; LI, P.; ZANG, S.; ZHANG, Y.; SONG, Y. Low-dimensional sn-based perovskites: Evolution and future prospects of solar cells. **Chem**, Elsevier, 2022.

# APPENDIX A – THEORETICALLY CALCULATED Γ-POINT PHONON MODES

| mode | wavenumber | irrep | classification | IR intensity | mode | wavenumber | irrep | classification | IR intensity |
|---|---|---|---|---|---|---|---|---|---|
| 1 | 45.46i | B3g | octahedron L | 0.0 | 88 | 985.03 | Au | $\tau$(NH2) | 0.0 |
| 2 | 39.60i | B1g | octahedron L | 0.0 | 89 | 986.32 | B3g | $\tau$(NH2) | 0.0 |
| 3 | 30.85i | Au | DMA L | 0.0 | 90 | 989.04 | B1g | $\tau$(NH2) | 0.0 |
| 4 | 20.56i | B2g | octahedron L | 0.0 | 91 | 997.51 | Ag | $\nu_{as}$(CNC) | 0.0 |
| 5 | 3.61i | B2u | accoustic T | 0.0162 | 92 | 999.02 | B3u | $\nu_{as}$(CNC) | 0.9201 |
| 6 | 3.56i | B3u | accoustic T | 0.0 | 93 | 1001.74 | B2g | $\nu_{as}$(CNC) | 0.0 |
| 7 | 2.12i | B1u | accoustic T | 0.0002 | 94 | 1002.78 | B1u | $\nu_{as}$(CNC) | 0.6639 |
| 8 | 13.71 | B1g | octahedron L | 0.0 | 95 | 1050.93 | B2g | $\rho$(CH3) | 0.0 |
| 9 | 15.16 | B2u | DMA L | 0.8015 | 96 | 1051.28 | Ag | $\rho$(CH3) | 0.0 |
| 10 | 20.80 | Au | DMA L + DMA T | 0.0 | 97 | 1054.13 | B3u | $\rho$(CH3) | 0.0338 |
| 11 | 22.91 | B1u | octahedron T | 0.0223 | 98 | 1055.21 | B1u | $\rho$(CH3) | 0.011 |
| 12 | 23.09 | B3g | octahedron L | 0.0 | 99 | 1213.98 | B1u | $\rho$(CH3) | 1.8009 |
| 13 | 25.50 | Ag | octahedron L | 0.0 | 100 | 1215.67 | B3u | $\rho$(CH3) | 0.0057 |
| 14 | 32.32 | B3u | octahedron T | 0.0595 | 101 | 1216.8 | B2g | $\rho$(CH3) | 0.0 |
| 15 | 40.74 | Au | octahedron v6(T2u) | 0.0 | 102 | 1218.48 | Ag | $\rho$(CH3) | 0.0 |
| 16 | 48.27 | B2u | octahedron L | 0.0605 | 103 | 1224.2 | B1g | $\rho$(CH3) | 0.0 |
| 17 | 50.98 | B1u | DMA T | 0.4937 | 104 | 1227.55 | Au | $\rho$(CH3) | 0.0 |
| 18 | 51.55 | B1g | DMA L | 0.0 | 105 | 1227.65 | B3g | $\rho$(CH3) | 0.0 |
| 19 | 52.84 | B3u | DMA L | 0.0647 | 106 | 1229.49 | B2u | $\rho$(CH3) | 1.7349 |
| 20 | 53.21 | B3g | DMA L | 0.0 | 107 | 1323.05 | Au | $\rho$(CH3) | 0.0 |
| 21 | 54.75 | B3u | DMA T | 0.9624 | 108 | 1324.59 | B2u | $\rho$(CH3) | 0.0573 |
| 22 | 55.78 | Ag | DMA L | 0.0 | 109 | 1326.29 | B1g | $\rho$(CH3) | 0.0 |
| 23 | 61.53 | B1u | DMA T | 0.0037 | 110 | 1327.82 | B3g | $\rho$(CH3) | 0.0 |
| 24 | 65.34 | B2g | DMA T | 0.0 | 111 | 1362.00 | Ag | $\omega$(NH2) | 0.0 |
| 25 | 68.45 | B3g | DMA L | 0.0 | 112 | 1364.05 | B2g | $\omega$(NH2) | 0.0 |
| 26 | 68.85 | B1g | DMA L | 0.0 | 113 | 1372.33 | B3u | $\omega$(NH2) | 2.4821 |
| 27 | 71.47 | Ag | DMA T | 0.0 | 114 | 1373.57 | B1u | $\omega$(NH2) | 2.9324 |
| 28 | 75.24 | Au | DMA L | 0.0 | 115 | 1389.75 | B2g | $\delta_s$(CH3) | 0.0 |
| 29 | 75.34 | B2u | DMA L | 1.6445 | 116 | 1390.61 | Ag | $\delta_s$(CH3) | 0.0 |
| 30 | 76.08 | B2g | DMA L | 0.0 | 117 | 1391.19 | B1u | $\delta_s$(CH3) | 0.8077 |
| 31 | 80.70 | B1u | DMA L | 0.0688 | 118 | 1391.98 | B3u | $\delta_s$(CH3) | 1.4555 |
| 32 | 81.24 | Ag | octahedron v5(T2g) | 0.0 | 119 | 1414.35 | Ag | $\delta_s$(CH3) | 0.0 |
| 33 | 82.11 | B3g | DMA L | 0.0 | 120 | 1415.21 | B3u | $\delta_s$(CH3) | 1.5045 |
| 34 | 82.58 | B2u | DMA L | 0.1097 | 121 | 1415.54 | B2g | $\delta_s$(CH3) | 0.0 |
| 35 | 86.09 | B1g | DMA L | 0.0 | 122 | 1417.05 | B1u | $\delta_s$(CH3) | 1.773 |
| 36 | 86.70 | B2g | octahedron v5(T2g) | 0.0 | 123 | 1431.37 | Ag | $\delta_{as}$(CH3) | 0.0 |
| 37 | 88.95 | Au | octahedron v6(T2u) | 0.0 | 124 | 1432.07 | B2g | $\delta_{as}$(CH3) | 0.0 |
| 38 | 88.99 | B3u | octahedron v3(T1u) | 0.5434 | 125 | 1432.84 | B3u | $\delta_{as}$(CH3) | 4.3736 |
| 39 | 92.45 | B1u | octahedron v3(T1u) | 0.8451 | 126 | 1433.2 | B1u | $\delta_{as}$(CH3) | 3.3695 |
| 40 | 92.69 | B2u | DMA L | 4.5383 | 127 | 1434.01 | B1g | $\delta_{as}$(CH3) | 0.0 |
| 41 | 94.63 | B3u | DMA L | 0.1261 | 128 | 1434.07 | B3g | $\delta_{as}$(CH3) | 0.0 |
| 42 | 95.32 | B1g | octahedron v5(T2g) | 0.0 | 129 | 1437.71 | Au | $\delta_{as}$(CH3) | 0.0 |
| 43 | 97.25 | Ag | octahedron v5(T2g) | 0.0 | 130 | 1438.06 | B2u | $\delta_{as}$(CH3) | 0.7927 |
| 44 | 98.12 | B2g | octahedron v5(T2g) | 0.0 | 131 | 1442.48 | Ag | $\delta_{as}$(CH3) | 0.0 |

| | | | | | | | | | |
|---|---|---|---|---|---|---|---|---|---|
| 45 | 98.28 | Au | DMA L | 0.0 | 132 | 1443.03 | B3u | $\delta_{as}$(CH3) | 3.2854 |
| 46 | 100.07 | B3u | octahedron v5(T2u) | 0.8785 | 133 | 1445.77 | B1u | $\delta_{as}$(CH3) | 6.5102 |
| 47 | 100.94 | B1u | octahedron v5(T2u) | 0.068 | 134 | 1446.14 | B2g | $\delta_{as}$(CH3) | 0.0 |
| 48 | 106.23 | B2u | octahedron v5(T2u) | 0.2241 | 135 | 1453.79 | B3g | $\delta_{as}$(CH3) | 0.0 |
| 49 | 109.51 | B3g | DMA T | 0.0 | 136 | 1456.12 | Au | $\delta_{as}$(CH3) | 0.0 |
| 50 | 109.76 | Au | DMA T | 0.0 | 137 | 1457.09 | B1g | $\delta_{as}$(CH3) | 0.0 |
| 51 | 110.9 | B2g | DMA T | 0.0 | 138 | 1459.6 | B2u | $\delta_{as}$(CH3) | 7.0888 |
| 52 | 112.86 | B1u | DMA T | 3.3967 | 139 | 1579.78 | B1u | $\delta$(NH2) | 5.1951 |
| 53 | 116.5 | B3u | DMA T | 0.2432 | 140 | 1580.87 | B3u | $\delta$(NH2) | 1.5202 |
| 54 | 116.53 | Ag | DMA T | 0.0 | 141 | 1585.75 | B2g | $\delta$(NH2) | 0.0 |
| 55 | 128.04 | B3g | octahedron v2(Eg) | 0.0 | 142 | 1586.05 | Ag | $\delta$(NH2) | 0.0 |
| 56 | 128.88 | B1g | octahedron v2(Eg) | 0.0 | 143 | 2999.51 | Ag | $\nu_s$(CH3) | 0.0 |
| 57 | 134.92 | Ag | octahedron v2(Eg) | 0.0 | 144 | 2999.99 | B3u | $\nu_s$(CH3) | 0.303 |
| 58 | 141.56 | B2g | octahedron v2(Eg) | 0.0 | 145 | 3000.49 | B2g | $\nu_s$(CH3) | 0.0 |
| 59 | 167.65 | Ag | octahedron v1(Ag) | 0.0 | 146 | 3000.55 | B1u | $\nu_s$(CH3) | 0.0233 |
| 60 | 167.86 | B2g | octahedron v1(Ag) | 0.0 | 147 | 3010.9 | B3u | $\nu_s$(CH3) | 1.0715 |
| 61 | 169.77 | B1g | $\tau$(CH3) | 0.0 | 148 | 3011.73 | B2g | $\nu_s$(CH3) | 0.0 |
| 62 | 173.45 | B3g | $\tau$(CH3) | 0.0 | 149 | 3012.17 | B1u | $\nu_s$(CH3) | 0.0503 |
| 63 | 177.89 | B2u | $\tau$(CH3) | 0.0007 | 150 | 3012.32 | Ag | $\nu_s$(CH3) | 0.0 |
| 64 | 178.6 | Au | $\tau$(CH3) | 0.0 | 151 | 3096.86 | Au | $\nu_{as}$(CH3) | 0.0 |
| 65 | 194.39 | B3u | octahedron v4(T1u) | 5.9727 | 152 | 3096.99 | B1g | $\nu_{as}$(CH3) | 0.0 |
| 66 | 194.84 | B1u | octahedron v4(T1u) | 7.0285 | 153 | 3097.02 | B2u | $\nu_{as}$(CH3) | 0.3402 |
| 67 | 196.76 | B2u | octahedron v4(T1u) | 7.945 | 154 | 3097.03 | B3g | $\nu_{as}$(CH3) | 0.0 |
| 68 | 197.3 | Au | octahedron v4(T1u) | 0.0 | 155 | 3108.75 | Ag | $\nu_{as}$(CH3) | 0.0 |
| 69 | 198.95 | B1u | octahedron v4(T1u) | 0.0163 | 156 | 3109.01 | B3u | $\nu_{as}$(CH3) | 0.0 |
| 70 | 209.24 | B3u | octahedron v4(T1u) | 0.1061 | 157 | 3109.07 | B2g | $\nu_{as}$(CH3) | 0.0 |
| 71 | 253.97 | B1g | $\tau$(CH3) | 0.0 | 158 | 3109.15 | B1u | $\nu_{as}$(CH3) | 0.0002 |
| 72 | 256.61 | B2u | $\tau$(CH3) | 0.3068 | 159 | 3109.69 | B1g | $\nu_{as}$(CH3) | 0.0 |
| 73 | 256.64 | B3g | $\tau$(CH3) | 0.0 | 160 | 3109.9 | B2u | $\nu_{as}$(CH3) | 1.0147 |
| 74 | 260.86 | Au | $\tau$(CH3) | 0.0 | 161 | 3109.98 | Au | $\nu_{as}$(CH3) | 0.0 |
| 75 | 383.25 | B2g | $\delta$(CNC) | 0.0 | 162 | 3110.2 | B3g | $\nu_{as}$(CH3) | 0.0 |
| 76 | 383.65 | B3u | $\delta$(CNC) | 0.0295 | 163 | 3116.79 | B3u | $\nu_{as}$(CH3) | 0.0086 |
| 77 | 383.73 | B1u | $\delta$(CNC) | 0.0001 | 164 | 3116.98 | B1u | $\nu_{as}$(CH3) | 0.7167 |
| 78 | 384.89 | Ag | $\delta$(CNC) | 0.0 | 165 | 3117.39 | Ag | $\nu_{as}$(CH3) | 0.0 |
| 79 | 789.3 | B3g | $\rho$(NH2) | 0.0 | 166 | 3117.54 | B2g | $\nu_{as}$(CH3) | 0.0 |
| 80 | 789.62 | B1g | $\rho$(NH2) | 0.0 | 167 | 3209.68 | B1u | $\nu_s$(NH2) | 30.6809 |
| 81 | 790.28 | B2u | $\rho$(NH2) | 4.0147 | 168 | 3211.15 | Ag | $\nu_s$(NH2) | 0.0 |
| 82 | 791.58 | Au | $\rho$(NH2) | 0.0 | 169 | 3211.52 | B3u | $\nu_s$(NH2) | 8.7428 |
| 83 | 878.92 | B3u | $\nu_s$(CNC) | 0.3995 | 170 | 3213.19 | B2g | $\nu_s$(NH2) | 0.0 |
| 84 | 880.08 | Ag | $\nu_s$(CNC) | 0.0 | 171 | 3231.76 | B1g | $\nu_{as}$(NH2) | 0.0 |
| 85 | 880.38 | B1u | $\nu_s$(CNC) | 1.7863 | 172 | 3231.99 | B3g | $\nu_{as}$(NH2) | 0.0 |
| 86 | 882.22 | B2g | $\nu_s$(CNC) | 0.0 | 173 | 3235.86 | B2u | $\nu_{as}$(NH2) | 69.1423 |
| 87 | 984.99 | B2u | $\tau$(NH2) | 0.1102 | 174 | 3236.06 | Au | $\nu_{as}$(NH2) | 0.0 |